THESIS

Analysis of Quasar Environments using a Galaxy and Quasar Formation Model

MOTOHIRO ENOKI

Department of Earth and Space Science
Graduate School of Science
Osaka University

January 2003

THESIS

Analysis of Quasar Environments using a Galaxy and Quasar Formation Model

MOTOHIRO ENOKI

A dissertation submitted to
Department of Earth and Space Science
Graduate School of Science
Osaka University

January 2003

Abstract

In this thesis, we construct a unified semi-analytic model that includes both galaxy and quasar formation based on a hierarchical clustering scenario and apply this model to investigate environment of quasars, i.e. relations between quasars and underlying mass distribution, and relations between galaxies and quasars.

We assume that a supermassive black hole is fueled by accretion of cold gas and that it is a source of quasar activity during a major merger of the quasar host galaxy with another galaxy. Our semi-analytic model for the galaxy formation can reproduce not only observations of galaxies in the local universe, such as luminosity functions and the cold gas mass fraction in spiral galaxies, but also galaxy number counts and redshift distributions of galaxies in the Hubble Deep Field. We incorporate a quasar formation model in this galaxy formation model. Our quasar formation model can reproduce the observed relation between a supermassive black hole mass and a spheroid luminosity, the present black hole mass function and the quasar luminosity functions at different redshifts. Using this model, we investigate environmental properties of quasar.

First, we analyze the mean numbers of quasars and galaxies in a dark halo, which provide the relations among galaxies, quasars and dark halos. We find that the dependence of the mean numbers of quasars on halo mass is different from the dependence of the mean numbers of galaxies. The behavior of these quantities in our model suggests that the clustering properties of galaxies is not the same as those of quasars. This is because the spatial distributions of galaxies and quasars depend on the mean numbers of quasars and galaxies in a dark halo, and the mean number depends on the halo mass in a different way for galaxies and quasars. Then, using the mean numbers, we calculate the bias parameters of quasars and galaxies. We find that the evolution of the bias parameters of quasars is different from that of galaxies. In our model, both the formation efficiency of galaxies and quasars depends on the cold gas mass fraction and the galaxy merger rate in a dark halo. However, the quasar formation efficiency depends on galaxy merger rate more strongly and ,furthermore, depends on quasar lifetime.

Next, we show the galaxy number distribution function around quasars. At lower redshifts ($0.2 \lesssim z \lesssim 0.5$), most halos with quasars have at most several galaxies. This indicates that most quasars reside in groups of galaxies. On the other hand, at higher redshifts ($1 \lesssim z \lesssim 2$), the number of galaxies in a dark halo with quasars is from several to dozens; quasars reside in ranging from small groups of galaxies to clusters of galaxies. These results show that most quasars at higher redshifts reside in more various environments than at lower redshifts. In our model, we assume that galaxy major merger triggers quasar activity. Since galaxy merger rate has a maximum in halos corresponding to groups of galaxies, $\sim 10^{13} M_{\odot}$, our model predicts that most quasars populate in groups. This model prediction at lower redshifts is consistent with the observation at $z \lesssim 0.4$. The results at higher redshifts can be checked by statistics of galaxies around quasars which will be obtained in the future.

Finally, we analyze the spatial cross-correlation between quasars and galaxies. To do this, we combine our semi-analytic model of our galaxy and quasar formation with cosmological N-body simulation. Comparison of the quasar-galaxy cross correlation functions with the galaxy two-point correlation functions shows that quasars populate in a similar environment to the galaxies with $M_B - 5\log(h) < -19$ even in high redshifts.

Comparing these predictions with observations in the future will enable us to constrain our quasar formation model.

Contents

Chapter 1

Introduction

1.1 Purpose

Understanding the origins and evolutions of galaxies is one of the most important problems in astrophysics and astronomy. Although observational and theoretical studies on galaxy formation have progressed remarkably, many problems in galaxy formation have never been completely resolved. In the deep universe, it is known that there exists another important class of objects, called *quasars*. It is also important to understand processes of quasar formation, but the origins and evolutions of quasars have also never been completely resolved. So far, many studies on quasar formation have been carried out independently of galaxy formation problems. However, since observational evidence suggesting close relations between galaxies and quasars has increased, a unified model which includes the formations of both galaxies and quasars is required.

On the other hand, recently, 8m class telescopes, including the SUBARU telescope, have began their operations for investigation of the deep universe and large surveys of galaxy and quasar, such as the Slone Digital Sky Survey (SDSS), are advancing. Thus, we will be able to obtain more detailed information not only on the local universe but also on the deep universe. Then, many observational data about galaxies, quasars and relations between them will be obtained in the near future. In order to predict these properties and to interpret the observational data coming in the near future, a unified model which includes the formations of both galaxies and quasars based on the cosmological context is necessary.

In this thesis, we construct a unified model for galaxy and quasar formation based on the standard cosmological structure formation theory. Then, we investigate properties of quasars using this model to explore the possibility to constrain quasar formation processes by comparison with observational data that have been obtained until now and will be obtained in the near future. As explained in detail later, various physical processes are intricately involved in galaxy formation and quasar formation. Therefore, first, we construct galaxy formation model that can reproduce some fundamental observed properties in the local universe. Next, we incorporate a quasar formation model into this galaxy formation model and investigate properties of quasars.

1.2 The hierarchical clustering scenario

A galaxy consists of stars and gas. The galaxy contains also *dark matter*. Some galaxies themselves tend to clump together into groups or clusters. Since galaxies are the basic elements in the universe, we must consider the formation of galaxies in the framework of a cosmological structure formation scenario. The modern scenario of cosmological structure formation is as follows.

First, small amplitude Gaussian density fluctuations, which might be originated from quantum fluctuations in the very early universe, grows via the gravitational instability. As the density fluctuations grow, overdense regions break away from the background cosmological expansion. Then, they collapse and form bound virialized objects. Behavior of growth of density fluctuations depends on a cosmological model. In this thesis, we adopt the cold dark matter (CDM) model as a cosmological model because predictions of this model can explain a number of current observations of large scale structure of the universe and this is widely accepted as a standard model of structure formation. In the CDM model, the amplitude of the density fluctuations decreases with increasing with scales. Thus, virialized objects which are called *dark halos* start to form on smaller scales in the earlier stage. Then, they cluster gravitationally and merge together. Thus, they are successively incorporated into larger dark halos. Therefore, the structure formation scenario in the CDM universe is called the *hierarchical clustering scenario*.

Growth of dark halos is due to purely gravitational interactions. On the other hand, in order to form luminous objects, such as galaxies, baryonic gas processes play essential roles. The basic scenario of galaxy formation in the hierarchical clustering universe (e.g. White & Rees 1978; Blumenthal et al. 1984; Cole 1991; White & Frenk 1991) is as follows: Before an overdense region forms a bound virialized object, baryonic gas behaves almost identically to dark matter. Once a dark halo has formed, the gas within the halo is shock-heated to about its virial temperature and then cools via radiative process. The gas cooling is very efficient on galactic and sub-galactic scales and, in the absence of heating source, the gas is expected to lose its pressure support quickly and concentrate in the center of the dark halo. Then, eventually the cooled gas turns into stars. After stars form, massive stars with short lifetime explode as supernovae (SNe) and they heat up surrounding gas. In this process, they release metals into the gas and regulate the subsequent star formation process. This process is called supernova feedback. As the stars evolve, stellar populations in galaxies are varied and chemical enrichment of stars and gas advance. These processes affect luminosities and colors of galaxies. When dark halos merge together into the new common halo, the halo may have some galaxies. In this case, these galaxies lose their energy resulting from the dynamical friction and fall into the center of the common halo. They may eventually merge and form more massive galaxy if the time scales of the dynamical friction are short enough.

As explained above, various physical processes are intricately involved in galaxy formation. The evolution of dark matter distribution is now well understood, and the evolution of individual stars is also mostly understood once they have formed. However, there are still very poorly understood processes of gaseous components evolution, such as star formation and feedback.

1.3 What is a quasar ?

Besides the problems of galaxy formation, problems on quasar formation have been also completely unsolved. The first discovery of quasars was brought by identifying optical counterparts of radio sources. It was initially believed that quasars were some strange new kind of stars in the Milky Way because they appeared as stellar-like point sources. Schmidt (1963) found that quasars were not Galactic stars but extragalactic objects because of their enormous redshifted line features. Estimating their distances using observed redshift and flux, it was found that luminosity of the quasar is more than about 10^{45}erg s^{-1}, and is brighter than 100 or more times luminosity of typical galaxies. It is possible to estimate the size of region emitting the radiation from the changing timescale of the radiation pattern. It turns out that the energy from the quasar is emitted from a very compact region, about 10^{15}cm, corresponding to the size of the solar system. It is impossible to produce high luminosity of quasars from such a compact region by nuclear fusion occurred in stars.

It has been widely accepted that quasars are luminous active galactic nuclei (AGN), and that they are fueled by accretion of gas onto supermassive black holes (SMBHs) in the nuclei of host galaxies since Lynden-Bell (1969) proposed. Because infalling gas into the galactic center has non-zero angular momentum, it forms an accretion disk. The viscosity in the disk causes the gas to lose angular momentum and hence spiral into the SMBH. The viscosity also heats up the disk, and then this heat energy is radiated away. In order to maintain the quasar activity, a large amount of gas needs to fall continuously into the central black hole. The black hole then grows if supply of gas is enough. However, a quasar will cease to radiate when the gas fueling stops. Most elliptical galaxies and massive bulge of spiral galaxies in nearby universe seem to contain SMBHs. This suggests that such galaxies experienced the quasar phase in a stage with their evolution.

While the understanding of the physical processes in quasars has made remarkable progress, fundamental problems, that is, how and when quasars were formed and how the quasar formation to the galaxy formation is related, are still not completely answered.

1.4 Relations between quasars and galaxies

In the recent years, there has been mounting observational evidence that the evolution of quasars and galaxies are closely related. It is observationally suggested that the evolution of quasar luminosity density shows a striking similarity to the evolution of the cosmic star formation rate and the spatial density of starburst galaxies. As well as the cosmic star formation rate, the redshift distribution of quasars has a maximum at $z \sim 2$ (Boyle & Terlvechi 1998; Franceschini et al. 1999). This similarity suggests that the mechanism of producing quasar activity is closely related to star formation processes. Observations of stellar kinematics in galactic centers suggest that many nearby galaxies have central black holes, and that their estimated masses correlate with the properties of spheroids[1] of their host galaxies. The estimated mass of SMBH in a galactic center is in proportion to the mass of the spheroid. The ratio of $M_{\rm BH}/M_{\rm spheroid}$ is $0.001 - 0.006$ in each galaxy (e.g.

[1]Throughout this thesis, we refer to bulge or elliptical galaxy as *spheroid*.

Kormendy & Richstone 1995; Magorrian et al. 1998; Merritt & Ferrarese 2001b). The ratio correlates with the velocity dispersion of stars in the spheroid as $M_{\rm BH} \propto \sigma^n_{\rm spheroid}, n = 3.7 - 4.7$ (e.g. Gebhardt et al. 2000; Merritt & Ferrarese 2001a). The connection between SMBHs and their host spheroids suggests that the formation of SMBHs physically links to the formation of the spheroids that harbor the SMBHs. Moreover, the observed images of quasar host galaxies show that they are mostly elliptical galaxies or bulge-dominated galaxies (e.g. Bahcall et al. 1997; McLure et al. 1999). These findings imply that the formation of quasars, the growth of SMBHs and the evolution of galaxies, especially of formation of spheroids, are all closely linked. Thus, the quasar formation should be analyzed together with the galaxy formation.

So far, many studies on quasar formation problems based on the hierarchical clustering scenario have been carried out with an assumption that the formation of quasars is linked not to the host galaxies but to the first collapse of dark matter halos with galactic mass, although these models can explain the decline of the quasar number density at $z \gtrsim 2$ (e.g. Efstathiou & Rees 1988; Haehnelt & Rees 1993) and properties of luminosity functions of quasars (e.g. Haiman & Loeb 1998; Haehnelt, Natarajan & Rees 1998; Hosokawa et al. 2001). Since quasars are directly linked to spheroids of host galaxies rather than to dark matter halos, the approximation of the one-to-one relation between quasar hosts and dark matter halos would be very crude, especially at low redshift. Therefore, in order to study the formation of quasars, it is necessary to construct a model related to the formation of galaxies, especially of spheroids, directly.

1.5 Semi-analytic models of galaxy formation

As previously mentioned, various physical processes are involved in the formation of galaxies. In order to predict properties of galaxies, direct numerical simulations that include the effects of gravity and the hydrodynamics in the cosmological context have been specifically developed (e.g. Cen & Ostriker 2000; Pearce et al. 2001). However, even with the best computer facility available today, the calculation accuracy is not still sufficient to resolve the formation and internal structure of individual galaxies in the cosmological numerical simulations. Furthermore, since some physical processes, like star formation and supernova feedback, are very poorly understood in details, phenomenological models are required to include such processes even in the simulations. Recently, a complementary approach to modeling galaxy formation in the CDM universe has been developed. This approach is referred to as *semi-analytic models* (SAMs) of galaxy formation.

In the CDM universe, since the mass fraction of baryonic component is small ($\sim 10\%$ to the total mass), the dynamics of dark matter plays an important role in structure formations. Therefore, in the SAMs, we divide galaxy formation processes into the following two step. First is virialization and hierarchical merging of dark halos, and second is evolution of baryonic components within the dark halos. At the first step, the merging histories of dark halos are realized using a Monte-Carlo algorithm or N-body simulation, and in the second step the evolution of baryonic components within dark halos is calculated using simple analytic models for gas cooling, star formation, supernova feedback, and other mechanisms. Stellar population synthesis models are used to calculate the lu-

minosities and colors of each galaxy. It is therefore straightforward to understand how galaxies form and evolve within the context of this model. An important advantage of SAMs is its flexibility. This allows the effects of varying assumptions or parameter choices to be readily investigated, and makes it possible to calculate a wide range of observable properties. SAMs successfully have reproduced a variety of observed features of galaxies in the local universe such as their luminosity functions, color distribution, and so on (e.g. Kauffmann, White & Guiderdoni 1993; Cole et al. 1994, Cole et al. 2000; Somerville & Primack 1999; Nagashima, Gouda & Sugiura 1999; Nagashima et al. 2001, Nagashima et al. 2002).

In these models, it is assumed that cooled gas in the halo forms disk stars. If two galaxies of comparable mass merge, it is assumed that starbursts occur and form the spheroid component. Numerical simulations have shown that the merger of galaxies can make spheroids and well reproduce their internal structure in detail (e.g. Barnes 1988; Hernquist 1992, Hernquist 1993; Heyl, Hernquist & Spergel 1994). Kauffmann & Charlot (1998) have demonstrated that the merger scenario for the formation of elliptical galaxies is consistent with the color-magnitude relation and its redshift evolution (see also Nagashima & Gouda 2001). Moreover, it has been also shown that the morphology-density relation for the elliptical galaxies in clusters of galaxies can be reproduced by such a merger hypothesis (Okamoto & Nagashima 2001a, Okamoto & Nagashima 2001b; Diaferio et al. 2001; Springel et al. 2001). Thus, we consider that this merger hypothesis for the origin of spheroids is acceptable. On the other hand, hydrodynamical simulations have shown that a merger of galaxies drives gas onto fall rapidly to the center of the merged system and to fuel nuclear starburst (Negroponte & White 1983; Mihos & Hernquist 1994, Mihos & Hernquist 1996; Barnes & Hernquist 1996). This suggests that the galaxy merger is a trigger for quasar activity. Moreover, observed images of quasar hosts show that many quasars reside in interacting systems or elliptical galaxies (Bahcall et al. 1997; McLure et al. 1999). Therefore, it is thought that the major merger of galaxies would be a possible mechanism for quasar and spheroid formation. Kauffmann & Haehnelt (2000) introduced a unified model that includes the formation of both galaxies and quasars within the framework of the SAM (see also Cattaneo 2001). They assumed that SMBHs are formed and fueled during the major mergers of galaxies, and their model quantitatively reproduced the observed relation between spheroid luminosity and black hole mass in nearby galaxies, the strong evolution of the quasar population with redshift, and the relation between the luminosities of nearby quasars and those of their host galaxies.

In this thesis, we investigate photometric and spatial properties of quasars, using a SAM incorporated a simple quasar formation model. We assume that SMBHs are formed and fueled during major galaxy mergers; the fueling process causes quasar activity. While this assumption is similar to the model of Kauffmann & Haehnelt (2000), our galaxy formation model and the adopted model of fueling process are different from their model. We use the model parameter set for galaxy formation that is determined by careful comparison with observations of galaxies in the local universe and that can reproduce the observational results of galaxy number counts and redshift distribution of galaxies in the Hubble Deep Field. Furthermore, we investigate other properties of quasars, to add to the properties considered by Kauffmann & Haehnelt (2000).

1.6 Methodology

While there are many properties of quasars that should be resolved, we focus on the investigation of the environments of quasars, that is, where do quasars exist? This is because the environments of quasars provide important clues to the physical processes of their formation and also yield important information on the relations among the distributions of quasars, galaxies and underlying dark matter in the universe. Due to their very high intrinsic luminosities, quasars at a higher redshift are much easier to find than galaxies at a similar redshift. Therefore, quasars can be used as a probe of the large-scale structure of the universe at high redshift. However, it is not necessarily a trivial problem whether quasars trace the large-scale structure or not. For more than three decades, we have known that quasars are associated with enhancements in the spatial distributions of galaxies (Bahcall, Schmidt & Gunn 1969). Studies on the environments of quasars in the nearby universe ($z \lesssim 0.4$) have shown that quasars reside in environments ranging from small to moderate groups of galaxies rather than in rich clusters (e.g. Bahcall & Chokshi 1991; Fisher et al. 1996; McLure & Dunlop 2001). Furthermore, since very large surveys of quasar and galaxy, such as the SDSS, will provide deep imaging of the quasars and their surroundings, it will be possible to study the relationship between quasars and their local environments for a very large number of quasars. This line of investigation will undoubtedly yield important information on the relation between galaxy environments, interactions, and quasar activity.

In this thesis, we investigate environments of quasars using our SAM to explore the possibility to constrain quasar formation processes by comparison with observations. Since various physical processes are intricately involved in galaxy formation and quasar formation, we specify a galaxy formation model that can reproduce observations of galaxies in the local universe. Then, we incorporate a quasar formation model into this galaxy formation model and investigate properties of quasars. Here, we focus on optical properties of quasars and attempt to consider the number of quasars in a dark halo, the effective bias parameter of quasars, the number of galaxies around quasars and quasar-galaxy spatial correlation function as characterizations of environments of quasars. Then we explore the possibility to constrain quasar formation processes by comparison of the predictions of our model with observations that were obtained until now and will be obtained in the near future.

This thesis is organized as follows. In Chapter 2, we describe our SAM for galaxy formation. In Chapter 3, we introduce our quasar formation model. In Chapter 4, we present the our model results for the number of quasars per halo, effective bias parameter of quasars, the number of galaxies around quasars. In Chapter 5, we analyze the clustering galaxies around quasars. To calculate the correlation function, we incorporate our SAM into N-body simulation. In Chapter 6, we provide a summary and conclusion. In appendixes, we briefly review the hierarchal clustering structure formation theory.

Chapter 2

Model of Galaxy Formation

2.1 Overview

In the CDM universe, small dark halos form first and then merge together to form larger dark halos as time passes. In each of the merged dark halos, shock-heating of baryonic gas, radiative gas cooling, star formation, and supernova feedback occur. The cooled dense gas and stars constitute *galaxies*. These galaxies sometimes merge together in a common dark halo and more massive galaxies form. In figure 2.1, we present a schematic view of this galaxy formation scenario in the CDM universe. SAM involves known physical processes connected with the process of galaxy formation. Our treatment of each of these processes is described in following sections. In this subsection, we explain the procedure of how to make predictions for the observable properties of galaxies at the redshift of interest.

In the first place, we construct merging histories of dark halos (§2.2). The merging histories depend on the adopted cosmological model. Next, we consider baryonic matter evolution in each merging path of dark halo in a time step of the merging history as follows:

(i) When a dark halo is formed, baryonic gas in the halo is shock-heated and cooled via radiative process. The amount of cooled gas that forms disk is calculated (§2.3.1).

(ii) The mass of stars formed by cooled gas is calculated (§2.3.2).

(iii) The amount of gas reheated by supernova feedback is computed (§2.3.3).

(iv) Chemical enrichment of stars and gas is computed (§2.3.4).

(v) If the halo contains several galaxies, whether the galaxies merge or not is investigated. The merging timescales via the dynamical friction and random collisions are estimated (§2.4.1).

(vi) If a major merger of galaxies occurs, a starburst is caused and a spheroid is formed (§2.4.2).

(vii) Spectrophotometric evolutions of stellar population are calculated. The effect of dust extinction on galaxy luminosity is also considered (§2.5).

The above procedures are repeated until the redshift of interest. Adopted model parameters of cosmology and galaxy formation in this study are described in (§2.6).

Our present SAM analysis obtains essentially the same results as the previous SAM analyses (e.g. Kauffmann, White & Guiderdoni 1993; Cole et al. 1994, Cole et al. 2000; Somerville & Primack 1999), with minor differences in a number of details, although our SAM can reproduce not only observations of galaxies in the local universe, such as luminosity functions and the cold gas mass fraction in spiral galaxies, but also galaxy number counts and redshift distributions of galaxies in the Hubble Deep Field.

2.2 Merger tree

In the CDM universe, dark matter halos cluster gravitationally and merge together in a manner that depends on the adopted cosmological parameters and power spectrum of initial density fluctuations. This merging history of dark halos is often referred to as a *merger tree*. In order to construct merger trees, it is possible to use collisionless cosmological N-body simulations of nonlinear gravitational clustering directly. The advantage of this approach is that we can obtain spatial distributions of dark halos. Therefore, it provide a powerful tool to investigate the clustering of galaxies. The disadvantage is that the computational cost is expensive and the much computational time is still required. Thus, it is difficult to explore a wide range of models, or different realizations in the same models. Moreover, the spatial resolution is still insufficient to follow motions of galaxies in an individual dark halo. An alternative approach is Monte Carlo method. In this method, merger trees are realized using an analytical formalism which represents dark halo mass function and the distribution of progenitor halo masses. Although it does not provide the spatial distribution of dark halos, many realizations can be performed at a lower cost and faster compared with N-body simulations. In this section, we describe the method of Monte Carlo realization of merger tree based on the analytical formalism called the *extended Press-Schechter Formalism* developed by Bower (1991), Bond et al. (1991) and Lacey & Cole (1993). The method using N-body simulations is introduced in Chapter 5.

Strictly speaking, in order to realize merger trees, one must know the conditional joint-probability distribution function of a set of halos mass M_2^j at time t_2 that are progenitors of a halo with mass M_1 at time t_1 ($M_2 < M_1$, $t_2 < t_1$) as follows:

$$P(M_2^1, M_2^2, \cdots, M_2^j, \cdots; t_2 | M_1; t_1) dM_2^1 dM_2^2 \cdots dM_2^j \cdots . \tag{2.2.1}$$

However, only the conditional one-point mass distribution function, $P(M_2, t_2|M_1, t_1)dM_2$, is obtained in the extended Press-Schechter formalism described in Appendix C. Therefore, it is not a trivial problem to realize merger trees. There are several methods to realize merger trees by Monte Carlo modeling based on the extended Press-Schechter formalism (e.g. Kauffmann & White 1993, Cole et al. 2000, Somerville & Kolatt (1999)). These methods can reconstruct the mean quantities analytically derived from the extended Press-Schechter formalism. In this thesis, we adopt the method developed by Somerville & Kolatt (1999) because their algorithm has practical advantages: it is simple and computationally efficient, and can be quickly performed.

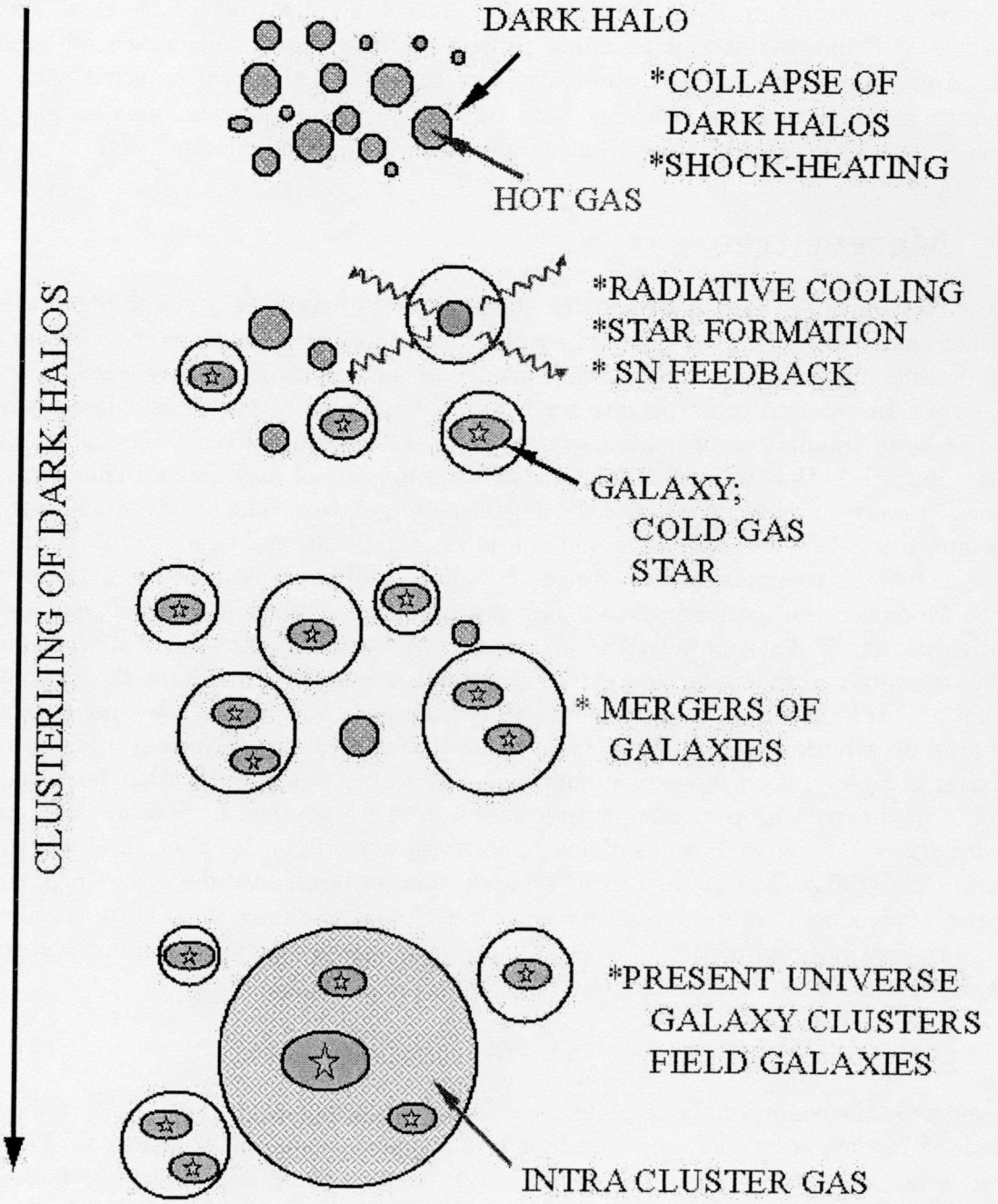

Figure 2.1: A schematic view of the galaxy formation scenario in the cold dark matter (CDM) universe. In this figure, cosmic time elapses from top to bottom.

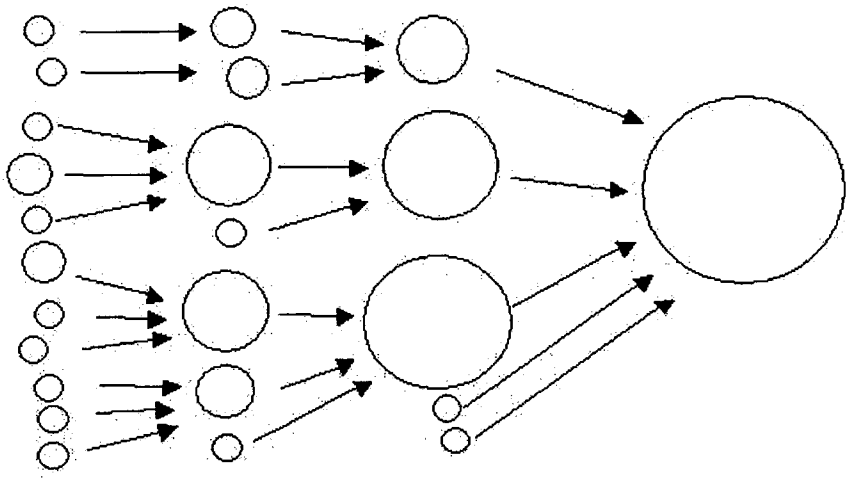

Figure 2.2: A schematic representation of a merger tree of dark halos. Circles show dark halos. In this figure, cosmic time elapses from left-hand to right-hand. However, Monte Carlo realization of merger tree is made from right-hand to left-hand.

The following procedure is based on Somerville & Kolatt (1999). First, we begin with a halo mass of M_1 at time t_1 and consider its progenitors at earlier time $t_2 = t_1 - \Delta t(t_1)$ where $\Delta t(t_1)$ is a time step. By using equation (C.2.1), we pick out M_2 randomly. Note that equation (C.2.1) is a simple Gaussian distribution, if we change the variable to $x \equiv (\sigma_2^2 - \sigma_1^2)/(\delta_{c2} - \delta_{c1})$. This M_2 is interpreted as a mass of a progenitor halo of the halo with M_1, collapsing at time t_2. If M_2 is less than $M_{\rm min}$, where $M_{\rm min}$ is a minimum mass for an object identified as an isolated halo at a corresponding time, the mass M_2 is considered as diffuse *accretion mass*. We repeat this process until the rest mass of the halo becomes less than $M_{\rm min}$. Next, each progenitor halo now become a starting halo, and we set a new time step and repeat the whole process in the same way until all masses picked out by equation (C.2.1) are less than the resolution mass, $M_{\rm min}$.

In this thesis, we adopt the power spectrum for the CDM universe from Bardeen et al. (1986) (see Appendix B.2.1). We take the resolution mass $M_{\rm min}$ corresponding to the circular velocity, $V_{\rm circ} = 40$ km s^{-1}, and treat halos with $V_{\rm circ} < 40$ km s^{-1} as diffuse accretion matter. This condition comes from the estimate of Jeans mass ($\sim 10^{10} M_\odot$) in the ultraviolet background radiation field (e.g. Thoul & Weinberg 1996). The evolution of the baryonic component is followed until the output redshift coincides with the redshift interval of $\Delta z = 0.06(1+z)$, corresponding to the dynamical time scale of halos which collapse at redshift z. Note that Shimizu et al. (2002) recently pointed out that a much shorter timestep is required to correctly reproduce the mass function given by the Press-Schechter formalism. However, a serious problem exists only on small mass scales ($\lesssim 10^{11} M_\odot$). Thus, we use the above prescription of timestep.

After construction of a merger tree, a formation time and lifetime of each halo is assigned as follows. If a dark halo has no progenitor halo, the formation time of the halo is defined by its collapse time. The end point of the halo's lifetime is defined as

the epoch when a halo mass becomes more than double of the mass at the formation time throughout subsequent mergers. Consistent with this definition, the formation time of newly formed halo is defined as the epoch when mergers produce a halo whose mass exceeds twice the mass of the most massive progenitor.

2.3 Gas and stars

2.3.1 Gas cooling

The baryonic gas mass fraction of each dark halo that has no progenitor halo and a diffuse accretion matter is given by $\Omega_{\rm b}/\Omega_0$, where $\Omega_{\rm b}$ is the baryonic density parameter constrained by primordial nucleosynthesis calculations. At the formation time of a dark halo, the gas in the halo is shock-heated to the virial temperature of the halo. We refer to this heated gas as the *hot gas*. The virial temperature of a halo with circular velocity $V_{\rm circ}$ is:

$$\begin{aligned} T_{\rm vir} &= \frac{1}{2}\frac{\mu m_{\rm p} V_{\rm circ}^2}{k_{\rm B}} \\ &= 35.9\left(\frac{\mu}{0.59}\right)\left(\frac{V_{\rm circ}}{1\ {\rm km\ s^{-1}}}\right)^2 {\rm K}, \end{aligned} \tag{2.3.1}$$

where μ is the mean molecular weight of the gas, $m_{\rm p}$ is the proton mass and $k_{\rm B}$ is the Boltzmann constant. Once the halo has formed, the hot gas in dense region of the halo cools due to efficient radiative cooling, sinks to the center of the halo and settle into a rotationally supported disk until the subsequent collapse of dark halo. We call this cooled gas the *cold gas*. This cold gas is a direct material for forming stars. Assuming that the hot gas is in collisional ionization equilibrium, the cooling timescale for the hot gas $\tau_{\rm cool}$ defined as the ratio of the thermal energy density of the hot gas to the cooling rate per unit volume is

$$\tau_{\rm cool} = \frac{3}{2}\frac{\rho_{\rm hot}(r)}{\mu m_{\rm p}}\frac{k_{\rm B}T_{\rm hot}}{n_{\rm e}^2(r)\Lambda(T_{\rm hot}, Z_{\rm hot})}, \tag{2.3.2}$$

where $\rho_{\rm hot}$ is the density of the gas at radius r, $n_{\rm e}$ is the number density of free electron, $T_{\rm hot}$ is the hot gas temperature (we assume $T_{\rm hot} = T_{\rm vir}$) and $\Lambda(T_{\rm hot}, Z_{\rm hot})$ is the cooling function for hot gas at temperature $T_{\rm hot}$ and with metallicity $Z_{\rm hot}$. Once the density distribution of the hot gas is specified, we can estimate the amount of the gas that has cooled by time t after the formation time of the dark halo. The cooling radius, $r_{\rm cool}$, is defined as a radius at which the cooling timescale, $\tau_{\rm cool}$, equals to the elapsed time from the formation time of the dark halo, t. The hot gas that distributes between $r_{\rm cool}(t)$ and $r_{\rm cool}(t + \Delta t)$ is cooled and added to the cold gas reservoir of the galaxy during time-step Δt.

In our SAM, assuming a singular isothermal density distribution of the hot gas, $\rho_{\rm hot}(r) \propto r^{-2}$, and using the metallicity-dependent cooling function by Sutherland & Dopita (1993), we calculate the amount of cold gas which eventually falls onto a central galaxy in the halo. In order to avoid the formation of unphysically large galaxies, the above cooling process is applied only to halos with $V_{\rm circ}$ <400 km s^{-1}. This handling would

be needed because the simple isothermal distribution forms so-called *monster galaxies* due to the too efficient cooling at the center of halos. While this problem will probably be solved by adopting another isothermal distribution with a central core (Cole et al. 2000), we take the above approach for simplicity.

2.3.2 Star formation

The cold gas that accumulates at the center of halo will eventually start to form stars. We assume that stars are formed from the cold gas at a rate of $\dot{M}_* = M_{\rm cold}/\tau_*$, where $M_{\rm cold}$ is the mass of cold gas and τ_* is the time scale of star formation. We assume that τ_* is independent of z, but dependent on $V_{\rm circ}$, as follows:

$$\tau_* = \tau_*^0 \left(\frac{V_{\rm circ}}{300{\rm km\ s^{-1}}} \right)^{\alpha_*} . \tag{2.3.3}$$

The free parameters of τ_*^0 and α_* are fixed by matching the observed mass fraction of cold gas in the neutral form in the disks of spiral galaxies. This scaling laws were first introduced by Cole et al. (1994). The free parameters of τ_*^0 and α_* are determined by matching the observed cold gas mass fraction in spiral galaxies. It should be noted that Cole et al. (2000) modified their original form (eq. [2.3.3]) as

$$\tau_* = \tau_*^0 \left(\frac{V_{\rm circ}}{200{\rm km\ s^{-1}}} \right)^{\alpha_*} \left[\frac{\tau_{\rm disk}(z)}{\tau_{\rm disk}(0)} \right] , \tag{2.3.4}$$

by multiplying a factor proportional to the dynamical timescale in the galactic disk, $\tau_{\rm disk}$. Nagashima et al. (2001) found that, although both models can reproduce the local luminosity function by adjustment of their free parameters, the latter model predicts too many high-z galaxies to be consistent with the observed redshift distribution of faint galaxies. This is because in the latter model more stars are formed at high redshift according to much a shorter τ_* as compared with the former model. Other recent SAM analysis on the evolution of damped Lyα systems (Somerville, Primack & Faber 2001) supports this result. Therefore, we adopt the former model (eq. [2.3.3]) as the star formation timescale.

2.3.3 Supernova feedback

Stars with masses larger than $10M_\odot$ explode as Type II supernovae (SNe), and then, they heat up the surrounding cold gas and drive it into the halo. The removal of cold gas from the galaxy acts as a feedback process, which regulates the star formation rate. This SN feedback reheats the cold gas to hot gas at a rate of $\dot{M}_{\rm reheat} = \beta \dot{M}_*$, where β is the efficiency of reheating. Since gas should be able to escape more easily from galaxies with smaller gravitational potentials, we assume that β depends on $V_{\rm circ}$, as follows:

$$\beta = \left(\frac{V_{\rm circ}}{V_{\rm hot}} \right)^{-\alpha_{\rm hot}} . \tag{2.3.5}$$

The free parameters of $V_{\rm hot}$ and $\alpha_{\rm hot}$ are determined by matching the local luminosity function of galaxies. With these $\dot{M}_*$ and $\dot{M}_{\rm reheat}$ thus determined, we obtain the masses

of hot gas, cold gas, and disk stars as a function of time during the evolution of galaxies (see §2.3.4).

2.3.4 Gas and chemical evolutions

Stars produce metals and release them into cold gas by stellar winds and SNe explosions. These metals become incorporated into later generations of stars and are also returned to hot gas in halos by SNe feedback. Since metal enrichment of the hot gas decreases the cooling timescale defined in equation (2.3.2), more gas can cool at later times. Metal enrichment of stellar component affects the color and the luminosity of stellar populations. We adopt a simple instantaneous recycling approximation (Tinsly 1980). In this approximation, we assume that all stars with masses smaller than $10M_{\odot}$ live forever whereas all stars larger than $10M_{\odot}$ die and eject material instantaneously. The gas and metal exchange is schematically shown in figure 2.3. The following differential equations describe the evolution of the mass of cold gas $M_{\rm cold}$, hot gas $M_{\rm hot}$, and long-lived stars $M_{\rm star}$ at each time step.

$$\dot{M}_{\rm cold} = -(1+\beta-R)\dot{M}_{*}, \tag{2.3.6}$$
$$\dot{M}_{\rm hot} = \beta\dot{M}_{*}, \tag{2.3.7}$$
$$\dot{M}_{\rm star} = (1-R)\dot{M}_{*}, \tag{2.3.8}$$

where $\dot{M}_{*} = M_{\rm cold}/\tau_{*}$ is star formation rate, β is the efficiency of reheating and R is the gas mass fraction returned from mass ejection by evolved stars to cold gas. The solutions of these equations are the following:

$$M_{\rm cold} = M^{0}_{\rm cold}\exp\left[-(1+\beta-R)\frac{t}{\tau_{*}}\right], \tag{2.3.9}$$
$$M_{\rm hot} = M^{0}_{\rm hot}+\beta\Delta M_{*}, \tag{2.3.10}$$
$$M_{\rm star} = M^{0}_{\rm star}+(1-R)\Delta M_{*}, \tag{2.3.11}$$

where $M^{0}_{\rm cold}, M^{0}_{\rm hot}$ and $M^{0}_{\rm star}$ are the masses of cold gas, hot gas and long-lived stars from the previous time step, t is the time since the start of the time step, and $\Delta M_{*} = (M^{0}_{\rm cold}-M_{\rm cold})/(1-R+\beta)$ is the mass of total formed stars. The differential equations for the evolution of the metallicity of cold gas $Z_{\rm cold}$ and hot gas $Z_{\rm hot}$ at each time step are:

$$M_{\rm cold}\dot{Z}_{\rm cold} = \alpha y(1-Z_{\rm cold})\dot{M}_{*}, \tag{2.3.12}$$
$$M_{\rm hot}\dot{Z}_{\rm hot} = \beta(Z_{\rm cold}-Z_{\rm hot})\dot{M}_{*}, \tag{2.3.13}$$

where y is yield and α is defined by $\alpha = 1-R$. The solutions of these equations are given as follows:

$$Z_{\rm cold} = 1-(1-Z^{0}_{\rm cold})\exp\left(-\alpha y\frac{t}{\tau_{*}}\right), \tag{2.3.14}$$

$$Z_{\rm hot} = 1-(1-Z^{0}_{\rm hot})\frac{M^{0}_{\rm hot}}{M_{\rm hot}} + \frac{M^{0}_{\rm cold}\beta(1-Z^{0}_{\rm cold})}{M_{\rm hot}\left[1+\beta-(R-\alpha y)\right]}\left\{\exp\left[-(1+\beta-(R-\alpha y))\frac{t}{\tau_{*}}\right]-1\right\}, \tag{2.3.15}$$

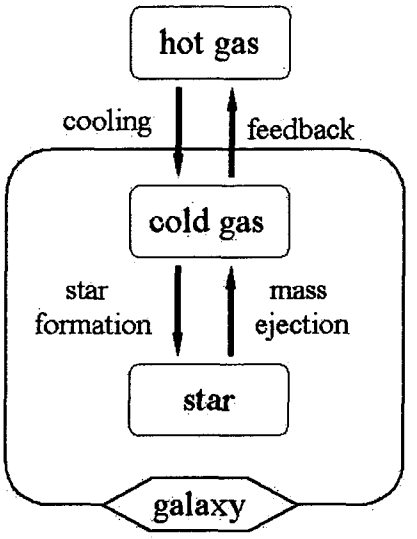

Figure 2.3: Schematic description of gas and metal recycling in star formation.

where $Z^0_{\rm cold}$ and $Z^0_{\rm hot}$ are the metallicities of cold gas and hot gas from the previous time step. The gas fraction returned by evolved stars, R, and yields, y, are chosen for a given stellar initial mass function (IMF).

2.4 Galaxy merging

2.4.1 Dynamical friction and random collisions

When several progenitor halos have merged, the newly formed larger halo should contain at least two or more galaxies which had originally resided in the individual progenitor halos. We identify the central galaxy of the most massive progenitor halo as the central galaxy of the new common halo. Other galaxies are regarded as satellite galaxies. These satellites lose energy and angular momentum due to the dynamical friction against the halo and spiral to the center of the halo. The timescale of the dynamical friction is given by

$$\begin{aligned} \tau_{\rm fric} &= f_{\rm merge}\frac{1.17}{\ln\Lambda_{\rm c}}\frac{R_{\rm H}^2 V_{\rm circ}}{GM_{\rm sat}} \\ &= f_{\rm merge}\frac{260}{\ln\Lambda_{\rm c}}\left(\frac{R_{\rm H}}{\rm Mpc}\right)^2\left(\frac{V_{\rm circ}}{10^3\ {\rm km\ s^{-1}}}\right)\left(\frac{M_{\rm sat}}{10^{12}\ M_\odot}\right)^{-1}{\rm Gyr}, \end{aligned} \tag{2.4.1}$$

where $f_{\rm merge}$ is a dimensionless parameter described below, $R_{\rm H}$ and $V_{\rm circ}$ are the radius and the circular velocity of the new common halo, respectively, $\ln\Lambda_{\rm c} \simeq \ln[1+(M_{\rm H}/M_{\rm sat})^2]$ is the Coulomb logarithm, $M_{\rm H}$ is the mass of the common halo, and $M_{\rm sat}$ is the mass of the satellite galaxy, including its dark matter halo (Binney & Tremaine 1987). Above derivation of the merger timescale is based on several assumptions (e.g. tidal stripping

of the satellite halo is ignored). Therefore, we introduce the parameter $f_{\rm merge}$ and adjust the time scale. Note that, since the halo dynamical timescale is $\tau_{\rm dyn} = R_{\rm H}/V_{\rm circ}$, the dynamical friction time scale is proportional to the halo dynamical timescale, $\tau_{\rm fric} \propto \tau_{\rm dyn} M_{\rm H}/(M_{\rm sat} \ln \Lambda_{\rm c})$. When the time elapsed after merging of progenitor halos exceeds $\tau_{\rm fric}$, the satellite galaxy is made to merge with the central galaxy. If the lifetime of the common halo is shorter than the time $\tau_{\rm fric}$, a new $\tau_{\rm fric}$ of new common halo is calculated and begins the whole process.

In addition, there will be collisions between satellite galaxies as they orbit within the halo. From a simple mean free path argument, satellites collide with the timescale $\tau_{\rm coll} \sim 1/n\sigma v$ where n is the mean density of galaxies, σ is the effective cross section for a single galaxy and v is a typical velocity of galaxy. From high-resolution N-body simulations, the mean free time scale of random collision is given by

$$\tau_{\rm coll} = \frac{500}{N^2}\left(\frac{R_{\rm H}}{\rm Mpc}\right)^3\left(\frac{r_{\rm gal}}{0.12\ {\rm Mpc}}\right)^{-2} \times\left(\frac{\sigma_{\rm gal}}{100\ {\rm km\ s^{-1}}}\right)^{-4}\left(\frac{\sigma_{\rm halo}}{300\ {\rm km\ s^{-1}}}\right)^3 {\rm Gyr}, \quad (2.4.2)$$

where N is the number of satellite galaxies, $r_{\rm gal}$ is their radius, and $\sigma_{\rm halo}$ and $\sigma_{\rm gal}$ are the 1D velocity dispersions of the common halo and satellite galaxies, respectively (Makino & Hut 1997). With a probability of $\Delta t/\tau_{\rm coll}$, where Δt is the timestep corresponding to the redshift interval Δz, a satellite galaxy merges with another randomly picked satellite. Note that since the collision timescale decreases with number of galaxies in the common halo, but increases with the common halo velocity dispersion, there will be a peak in the collision rate for a halo size about the mass of a group, $\sim 10^{13} M_\odot$. This process was first introduced in a SAM by Somerville & Primack (1999).

2.4.2 Spheroid formation

If two galaxies of comparable mass merge, it is assumed that starbursts occur and form the spheroidal component in the center of the galaxy. N-body simulations of collisions between equal mass disk galaxies have shown that a merger hypothesis for the origin of spheroids can explain their detailed internal structure (e.g. Barnes 1988; Hernquist 1992, Hernquist 1993; Heyl, Hernquist & Spergel 1994). Consider the case that two galaxies of masses m_1 and $m_2 (> m_1)$ merge together. If the mass ratio, $f = m_1/m_2$, is larger than a certain critical value of $f_{\rm bulge}$, we assume that a starburst occurs, and that all the cold gas turn into stars and hot gas, which fills the halo, and all of the stars populate the bulge of a new galaxy. In this case, the merger is called *major merger*. On the other hand, if $f < f_{\rm bulge}$, no starburst occurs and a smaller galaxy is simply absorbed into the disk of a larger galaxy. In this case, the merger is called *minor merger*.

When a starburst occurs, stars are formed in a very short timescale. Thus, the starburst corresponds to $\tau_*/t \to 0$ in equations (2.3.9)–(2.3.11). In this case, the masses after a starburst are given by

$$M_{\rm cold} = 0, \quad (2.4.3)$$

$$M_{\rm hot} = M^0_{\rm hot} + \frac{\beta M^0_{\rm cold}}{1+\beta-R}, \tag{2.4.4}$$

$$M_{\rm star} = M^0_{\rm star} + \frac{(1-R)M^0_{\rm cold}}{1+\beta-R} \tag{2.4.5}$$

and the total star mass formed at starburst becomes

$$\Delta M_{*,\rm burst} = \frac{M^0_{\rm cold}}{1+\beta-R}. \tag{2.4.6}$$

We classify galaxies into different morphological types according to the B-band bulge-to-disk luminosity ratio, B/D. In this thesis, following Simien & de Vaucouleurs (1986), galaxies with $B/D \geq 1.52$, $1.52 > B/D \geq 0.68$, and $B/D < 0.68$ are classified as ellipticals, S0s and spirals, respectively. The parameters of $f_{\rm merge}$ and $f_{\rm bulge}$ are determined by agreement with the ratio of observed morphological types.

2.5 Luminosity of galaxy

2.5.1 Stellar population synthesis

Given the star formation rate as a function of time, the absolute luminosity and colors of individual galaxies are calculated using a stellar population synthesis model. This model provides the Spectral Energy Distribution (SED) of a stellar population of a single age and metallicity per unit mass of stars, $\Phi_\lambda(t, Z)$. To compute $\Phi_\lambda(t, Z)$, we must choose the Initial Mass Function (IMF), which indicates the fraction of stars created with a given mass. The resulting SED of each galaxy, $L_\lambda(t)$, at time t is given by convolving the star formation rate with single stellar population SEDs:

$$L_\lambda(t) = \int_0^t \Phi_\lambda[t-\tau, Z_*(\tau)]\dot{M}_*(\tau)d\tau, \tag{2.5.1}$$

where $Z_*(t)$ is the metallicity of stars forming at time t, and $\dot{M}_*(t)$ is the star formation rate at that time. In the case of a galaxy which formed by merging, we also sum the contributions to $L_\lambda(t)$ from progenitor galaxies. We use the population synthesis code by Kodama & Arimoto (1997). The stellar metallicity grids in the code cover a range of $Z_* = 0.0001 - 0.05$. The IMF that we adopt is the power-law IMF of Salpeter form with lower and upper mass limits of $0.1{\rm M}_\odot$ and $60{\rm M}_\odot$, respectively. Since our knowledge of the lower mass limit is incomplete, there is the possibility that many brown dwarf-like objects are formed. Therefore, following Cole et al. (1994), we introduce a parameter defined as $\Upsilon = (M_{\rm lum} + M_{\rm BD})/M_{\rm lum}$, where $M_{\rm lum}$ is the total mass of luminous stars with $m \geq 0.1M_\odot$ and $M_{\rm BD}$ is that of invisible brown dwarfs.

2.5.2 Dust extinction

Since dust grains in the cold gas absorb and scatter light, they can significantly attenuate the optical luminosity of galaxies. The resultant SED of a galaxy is given by $L^{\rm dust}_\lambda =$

$f_{\rm att,\lambda}L_\lambda$. Here $f_{\rm att,\lambda}$ is the attenuation factor of galactic light, and it depends on the dust optical depth and the spatial distribution of dust in a galaxy. To account for extinction by dust in each galaxy, we adopt a simple model by Wang & Heckman (1996) in which the optical depth in B-band, τ_B, is related to the luminosity as $\tau_B = 0.8(L_B/1.3\times10^{10}L_\odot)^{0.5}$. The optical depths in other bands are calculated by using the galactic extinction curve, and the dust distribution in disks is assumed to be the slab model considered by Somerville & Primack (1999). In the slab model, it is assumed that stars and dust distribution are the same, and the attenuation factor is given by

$$f_{\rm att,\lambda} = \frac{1-\exp(-\tau_\lambda)}{\tau_\lambda} \tag{2.5.2}$$

where τ_λ is a dust optical depth. In this dust model, while the extinction in B band is typically $A_B = -2.5\log(f_{\rm att,B}) \sim 1$ mag at the bright end of the local luminosity function, our results in the K band are not significantly affected by the details of the dust model.

2.6 Setting parameters of the galaxy formation model

The above procedure is a standard one in the SAM for galaxy formation. Galaxy formation model parameters are determined by comparison with observations of galaxies in the local Universe. In this study, we use the galaxy formation model parameters determined by Nagashima et al. (2001) from observations of galaxies in the local universe such as luminosity functions and the cold gas mass fraction in spiral galaxies. The adopted parameters of this model are tabulated in table 2.1 and 2.2. The model with these parameters can reproduce galaxy number counts and photometric redshift distribution of galaxies in the Hubble Deep Field.

Before the galaxy formation parameters are determined, we must specify the cosmological parameters; the present density parameter, Ω_0, the cosmological constant, λ_0, the Hubble constant in units of 100 km s^{-1} Mpc^{-1}, h, and the present rms density fluctuation in spheres of $8h^{-1}$Mpc radius, σ_8. The cosmological model that we have chosen is a flat, low-density CDM model with a cosmological constant (ΛCDM model). The adopted parameters are tabulated in table 2.1. The ΛCDM model with this set of model parameters is currently favored by quite a range of observational evidence. The location of the first acoustic peak in the angular power spectrum of fluctuations in the temperature of the cosmic microwave background (CMB) implies that the universe is flat, $\Omega_0 + \lambda_0 \sim 1$ (e.g. de Bernardis et al 2002). The data on the distance-luminosity relation of type Ia SNe imply that $0.8\Omega_0 - 0.6\lambda_0 \sim -0.2$ (Perlmutter et al. 1999). The result from the Hubble Space Telescope Key Project to measure galaxy distance is $h \sim 0.7$ (Freedman et al 2001). The observations of the CMB temperature fluctuations on large scale imply that $\sigma_8 \sim 1$ (Bennett et al 1996). The adopted baryonic density parameter $\Omega_{\rm b} = 0.015h^{-2}$ is constrained by primordial nucleosynthesis calculations (e.g. Suzuki, Yoshii & Beers 2000). Note that a recent measurement of the anisotropy of the CMB by the BOOMERANG project suggests a slightly higher value, $\Omega_{\rm b} \sim 0.02h^{-2}$ (Netterfield et al. 2002). Cole et al. (2000) have already investigated the effect of changing $\Omega_{\rm b}$, and showed that this mainly affects the value of the invisible stellar mass fraction parameterized by Υ. We also checked

Table 2.1: Cosmological Model Parameters

Ω_0	λ_0	h	σ_8	Ω_b
0.3	0.7	0.7	1	0.03

whether our results are changed or not in the case of $\Omega_b \sim 0.02h^{-2}$ and found that this does not much affect them.

The galaxy formation model parameters are constrained as follows: First, the SN feedback-related parameters ($V_{\rm hot}$, $\alpha_{\rm hot}$) are determined by the location of the knee of the luminosity function and the faint-end slope, respectively. It should be noted that the mass fraction Υ of invisible stars determines the magnitude scale of galaxies, so that changing Υ moves the luminosity function horizontally without changing its overall shape. Therefore, coupled with $V_{\rm hot}$, Υ determines the bright portion of the luminosity function. In figure 2.4 we plot the results of local luminosity functions of galaxies represented by the solid lines. Note that the resultant luminosity functions hardly change if the SMBH formation model is included (dashed lines; see the Chapter 3). The symbols with errorbars indicate observational results from some B-band redshift surveys (APM, Loveday et al. 1992; 2dF, Folkes et al. 1999) and from some K-band redshift surveys (Gardner et al. 1997; 2MASS, Cole et al. 2001). As can be seen, the results of our model using these parameters are generally consistent with the observed local luminosity functions.

Next, the star formation-related parameters (τ_*^0, α_*) are determined by using the cold gas mass fraction in spiral galaxies. The gas fraction depends on both the SN feedback-related parameters and on the star formation related ones. The former parameters determine the gas fraction expelled from galaxies and the latter parameters determine the gas fraction that is converted into stars. Therefore, before determining the star formation-related parameters, the SN feedback-related parameters must be determined by matching the local luminosity function. Figure 2.5 shows the ratio of cold gas mass relative to the B-band luminosity of spiral galaxies as a function of their luminosity. The thick line shows the result of the model without SMBH formation and the short dashed line shows the model with SMBH formation. We here assume that 75% of the cold gas in these models is comprised of hydrogen, i.e., $M_{\rm HI} = 0.75M_{\rm cold}$. Open squares with error bars indicate the HI data, taken from Huchtmeier & Richter (1988). Since their data do not include the fraction of H_2 molecules, the observational result should be regarded as providing a lower limit of the cold gas mass fraction.

Finally, the merging-related parameters of $f_{\rm merge}$ and $f_{\rm bulge}$ are determined by matching the observed morphological type mix. The gas fraction returned by evolved stars, R, and yields, y, are chosen for the Salpeter IMF and determined by matching observed metallycity in galaxies. Comparison of model predictions with the observed galaxy number counts and photometric redshift distribution of galaxies in the Hubble Deep Field constrains star formation model as is mentioned in §2.3.2. Detailed analysis and discussions are described in Nagashima et al. (2001), Nagashima et al. 2002.

Table 2.2: Galaxy Formation Model Parameters

$V_{\rm hot}$ (km s^{-1})	$\alpha_{\rm hot}$	τ_*^0 (Gyr)	α_*	$f_{\rm merge}$	$f_{\rm bulge}$	R	y	Υ
280	2.5	1.5	-2	1	0.5	0.25	0.038	1.5

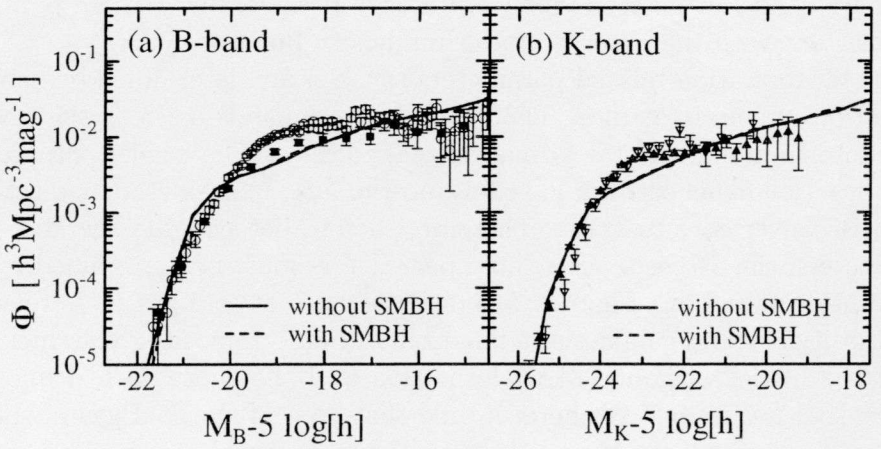

Figure 2.4: Local luminosity functions in the (a) B-band and (b) K-band. The thick line shows the result of the model without SMBH formation. The short dashed line shows the model with SMBH formation. The symbols with errorbars in (a) indicate the observational data from APM (Loveday et al. 1992, *filled squares*) and 2dF (Folkes et al. 1999, *open circles*). Symbols in (b) indicate the data from Gardner et al. (1997, *open inverted triangles*), and 2MASS (Cole et al. 2001, *filled triangles*).

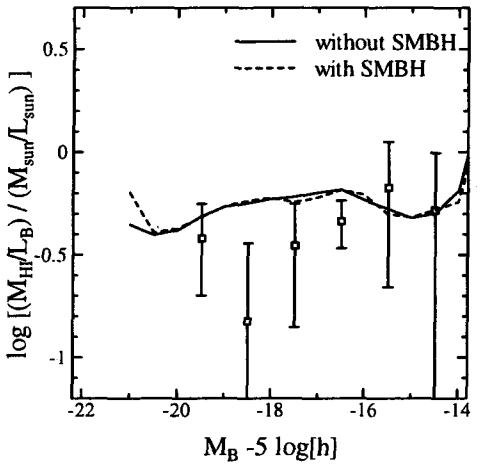

Figure 2.5: Cold gas mass relative to B-band luminosity of spiral galaxies. The thick line shows the result of the model without SMBH formation and the short dashed line shows the model with SMBH formation. The open squares with errorbars indicates the observational data for atomic hydrogen taken from Huchtmeier & Richter (1988). In the models, cold gas consists of all species of elements. Thus, we take $M_{\rm HI} = 0.75 M_{\rm cold}$, which corresponds to the fraction of hydrogen. Because the observational data denote only atomic hydrogen, they should be interpreted as lower limits of the ratio.

Chapter 3

Model of Quasar Formation

3.1 The growth of black hole

In this chapter, we introduce a quasar formation and evolution model into our SAM. As mentioned in Chapter 1, the masses of SMBHs have tight correlation with the spheroid masses of their host galaxies (e.g. Kormendy & Richstone 1995; Magorrian et al. 1998; Merritt & Ferrarese 2001b) and the hosts of quasars found in the local Universe are giant elliptical galaxies or galaxies displaying evidence of major mergers of galaxies (e.g. Bahcall et al. 1997; McLure et al. 1999). Moreover, in SAMs for galaxy formation, it is assumed that the major merger of galaxies leads to the formation of a spheroid. Therefore, we assume that SMBHs grow by merging, and are fueled by accreted cold gas during major mergers of galaxies. When host galaxies merge, pre-existing SMBHs sink to the center of the new merged galaxy owing to the dynamical friction, and finally coalesce. The timescale for this process is unknown, but for the sake of simplicity we assume that SMBHs merge instantaneously. Gas-dynamical simulations have demonstrated that the major merger of galaxies can drive substantial gaseous inflows and trigger starburst activity (Negroponte & White 1983; Mihos & Hernquist 1994, Mihos & Hernquist 1996; Barnes & Hernquist 1996). Thus, we assume that during a major merger, some fraction of the cold gas that is proportional to the total mass of stars newly formed at starburst is accreted onto the newly formed SMBH. Under this assumption, the mass of cold gas accreted on a SMBH is given by

$$\begin{aligned} M_{\rm acc} &= f_{\rm BH}\Delta M_{*,\rm burst} \\ &= f_{\rm BH}\frac{M^0_{\rm cold}}{1+\beta-R}, \end{aligned} \tag{3.1.1}$$

where $f_{\rm BH}$ is a constant and $\Delta M_{*,\rm burst}$ is the total mass of stars formed at starburst. $\Delta M_{*,\rm burst}$ is derived in §2.4.2. The gas recycling for the model including SMBH formation is schematically shown in figure 3.1. The free parameter of $f_{\rm BH}$ is fixed by matching the observed relation between a spheroid luminosity and a black hole mass found by Magorrian et al. (1998); we find that the favorable value of $f_{\rm BH}$ is nearly 0.03. In figure 3.2 we show scatterplots (open circles) of the absolute V-band magnitudes of spheroids versus the masses of SMBHs of the model for $f_{\rm BH} = 0.03$. The thick solid line is the observational

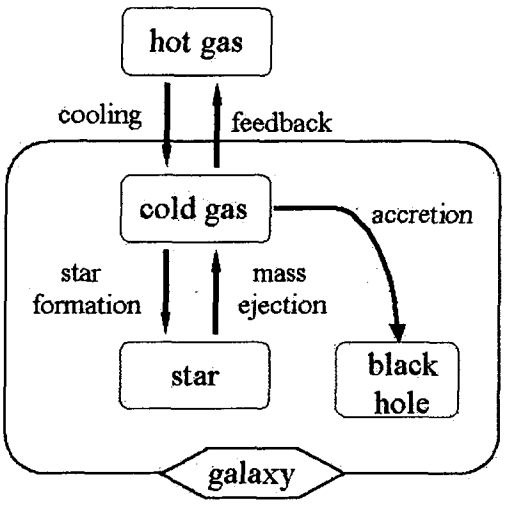

Figure 3.1: Schematic description of gas recycling in burst star formation including black hole formation.

relation and the dashed lines are the 1σ scatter in the observations obtained by Magorrian et al. (1998). The obtained gas fraction ($f_{\rm BH} = 0.03$) is so small that the inclusion of SMBH formation does not change the properties of galaxies in the local Universe. In figure 2.4 and 2.5, the dashed lines show the results of the model with SMBH formation. This result differs negligibly from the result of the model without SMBH formation. Therefore, we use the same galaxy formation parameters tabulated in table 2.2 regardless of including the SMBH formation model. Figure 3.3 (a) shows the black hole mass functions in our model at a series of redshifts. This indicates that the number density of the most massive black holes increases monotonically with time in the scenario where SMBHs grow by the accretion of cold gas and by merging. In figure 3.3 (a), we superpose the present black hole mass function obtained by Salucci et al. (1999). They derived this black hole mass function from the observed radio luminosity function of nearby radio-quiet galaxies and the empirical correlation between radio luminosities from the nuclei of radio-quiet galaxies and the mass of their black holes. The present mass function in our model is consistent with the mass function obtained by Salucci et al. (1999). For a comparison, we also plot the mass functions of the bulge and disk for all galaxies in figure 3.3 (b) and (c), respectively. The steep slopes at low masses of the mass functions of black hole and bulge are mainly due to random collisions between satellite galaxies in this model. For $f_{\rm BH} \lesssim 0.3$, varying $f_{\rm BH}$ shifts the black hole mass almost linearly. This tendency is shown in Figure 3.4.

3.2 Evolution of quasar luminosity

Next, we consider the light curve of quasars. In this study, we define a quasar as a galaxy with the SMBH which is powered during the major merger of galaxies in the manner described in the previous section. We assume that a fixed fraction of the rest mass energy

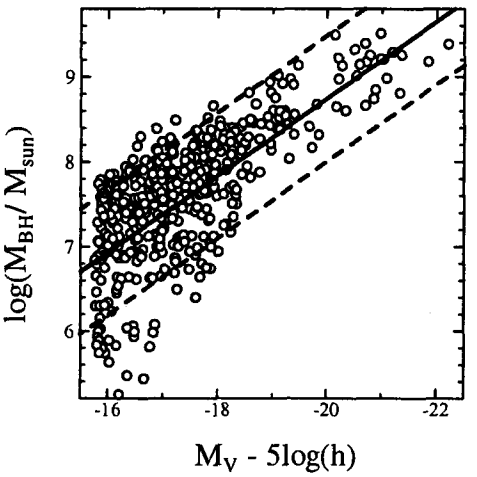

Figure 3.2: Relation the absolute V-band spheroid magnitude to mass of SMBH. The open circles are an absolute V-band magnitude limited sample of spheroids in our model. The thick solid line is the observational relation obtained by Magorrian et al. (1998). The dashed lines indicate the 1σ scatter in the observations.

of the accreted gas is radiated in the B-band, and that the B-band luminosity of a quasar at time t after a major merger as follows:

$$L_B(t) = L_B(\text{peak}) \exp(-t/t_{\text{life}}), \tag{3.2.1}$$

where $t_{\text{life}}(z)$ is the quasar lifetime. We assume that $t_{\text{life}}(z)$ scales with the dynamical time scale, t_{dyn}, of the host galaxy, where $t_{\text{dyn}} \propto r_{\text{gal}}/\sigma_{\text{gal}} \propto R_{\text{H}}/V_{\text{circ}} \propto \Delta_{\text{vir}}^{-1/2}$; Δ_{vir} is the ratio of the dark halo density to the present critical density given in Appendix B.3. The peak luminosity, $L_B(\text{peak})$, is given by

$$\begin{aligned} L_B(\text{peak}) &= \frac{\epsilon_B M_{\text{acc}} c^2}{t_{\text{life}}}, \\ &= 1.49 \times 10^{13} \epsilon_B \left(\frac{M_{\text{acc}}}{10^7 M_\odot}\right) \left(\frac{t_{\text{life}}}{10^7 \text{yr}}\right)^{-1} L_\odot \end{aligned} \tag{3.2.2}$$

where ϵ_B is the radiative efficiency in the B-band, t_{life} is the quasar lifetime and c is the speed of light. The absolute B-band magnitude at the peak $M_B(\text{peak})$ is given by:

$$M_B(\text{peak}) = -2.5 \log \left[\epsilon_B \left(\frac{M_{\text{acc}}}{10^7 M_\odot}\right) \left(\frac{t_{\text{life}}}{10^7 \text{yr}}\right)^{-1}\right] - 27.45. \tag{3.2.3}$$

In order to determine the parameter ϵ_B and the present quasar lifetime, $t_{\text{life}}(0)$, we chose them to match the estimated luminosity function in our model with the observed abundance of bright quasars at $z = 2$. We obtain $\epsilon_B = 0.0048$ and $t_{\text{life}}(0) = 3.0 \times 10^7$yr. The resulting luminosity functions at four different redshifts are shown in figure 3.5. We superpose the luminosity functions derived from the 2dF 10k catalogue (Croom et al.

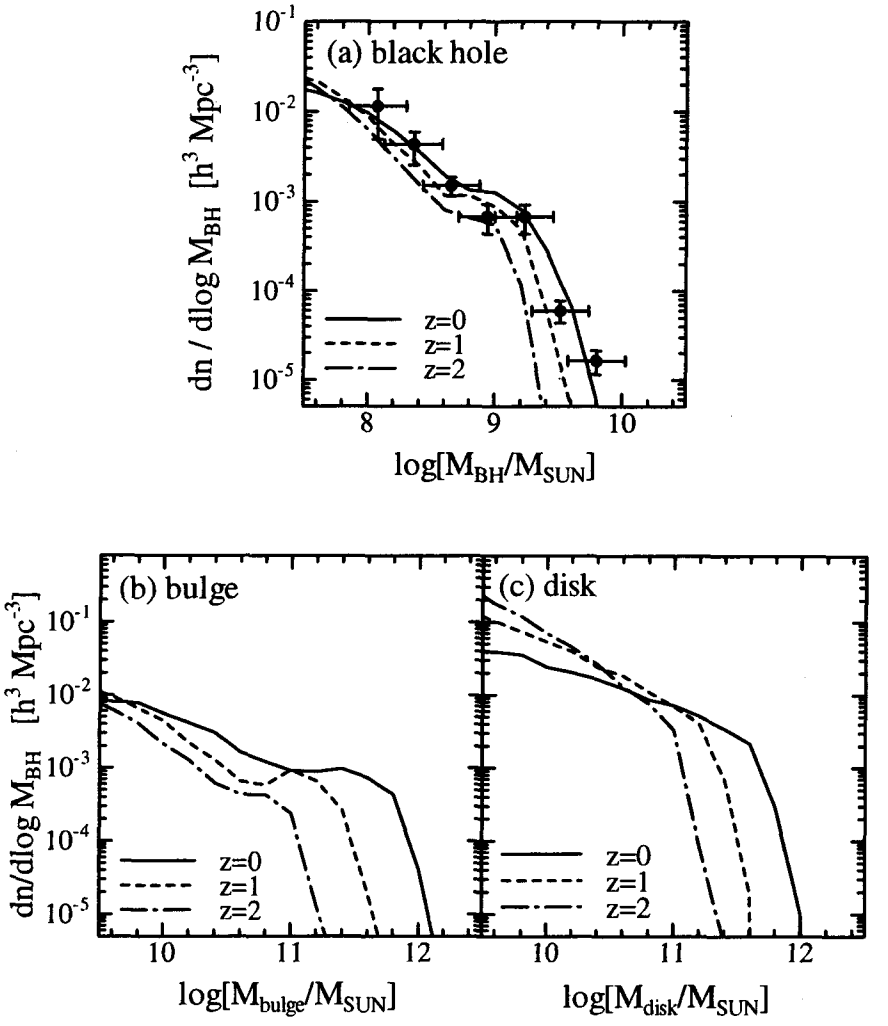

Figure 3.3: (a) Black holes mass function of models for $f_{\rm BH} = 0.03$ as a function of the epoch. The solid, short-dashed, and dot-dashed lines indicate the results at $z = 0, 1,$ and 2, respectively. The symbols with errorbars are the present black hole mass function obtained by Salucci et al. (1999). (b) The bulge and (c) the disk mass functions of model galaxies as a function of the epoch. The solid, short-dashed, and dot-dashed lines indicate the results at $z = 0, 1,$ and 2, respectively.

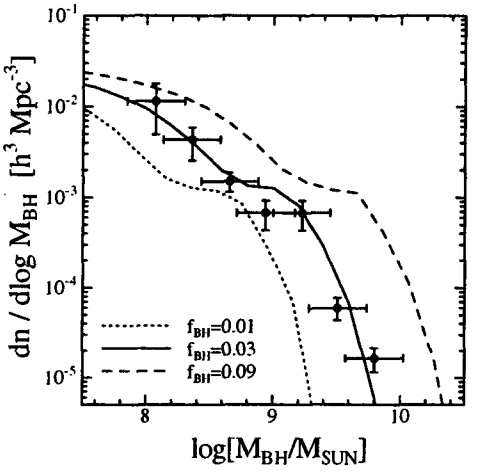

Figure 3.4: The effect on black hole mass functions of varying $f_{\rm BH}$. Results are shown for $f_{\rm BH} = 0.01$ (dotted line), $f_{\rm BH} = 0.03$ (solid line), and $f_{\rm BH} = 0.09$ (dashed line). The symbols with errorbars are the present black hole mass function obtained by Salucci et al. (1999).

2001) for a cosmology with $\Omega_0 = 0.3, \lambda_0 = 0.7$, and $h = 0.7$, which is analyzed and kindly provided by T. T. Takeuchi. He used the method of Efstathiou, Ellis & Peterson (1988) to estimate the luminosity functions. In order to reanalyze the error with greater accuracy, they applied bootstrap resampling according to the method of Takeuchi, Yoshikawa & Ishii (2000). The absolute B-band magnitudes were derived for quasars using the k-corrections derived by Cristiani & Vio (1990). Our model reproduces reasonably well the evolution of the observed luminosity functions. Thus, in the next chapter, we use these model parameters in order to investigate the environments of quasars (table 3.1).

For a comparison, we also plot the result of model with $\epsilon_B = 0.0048$ and $t_{\rm life}(0) = 3.0 \times 10^8$yr in figure 3.5 (dot-dashed lines). In this case, the abundance of luminous quasars decreases. To prolong the quasar lifetime affects the quasar luminosity function due to the following two factors: a decrease in the peak luminosity, $L_{\rm B}$ (eq.[3.2.2]), and an increase in the exponential factor, $\exp(-t/t_{\rm life})$, in equation (3.2.1). For the majority of bright quasars, the elapsed time, t, since the major merger is much smaller than the quasar lifetime $t_{\rm life}$, $t/t_{\rm life} \ll 1$. Therefore, the former factor dominates the latter, and the number of luminous quasars decreases. Thus, a long quasar lifetime results in a very steep quasar luminosity function. Note that if we change the radiative efficiency, ϵ_B, the quasar luminosities simply scale by a constant factor in our model. Thus, changing ϵ_B shifts the luminosity function horizontally.

Kauffmann & Haehnelt (2000) also introduced a unified model which includes the formation of both galaxies and quasars in the framework of SAM. In their model, they also assumed that SMBHs are formed and fueled during major mergers. While their approach is similar to ours, they adopted another model of fueling process. They assumed that the ratio of the accreted mass to the total available cold gas mass scales with halo circular velocity in the same way as the mass of stars formed per unit mass of cooling

Table 3.1: Quasar Model Parameters

$f_{\rm BH}$	ϵ_B	$t_{\rm life}(0)$ $(10^7{\rm yr})$
0.03	0.0048	3.0

gas. Therefore, their resultant model description is slightly different from ours in equation (3.1.1). Furthermore, their models for star formation and feedback are different from ours, and they did not consider random collisions. On the other hand, in our model, luminous quasars could reside inside a dark halo in three possible ways: (i) A major merger between a satellite and the central galaxy in the halo drives cold gas onto a SMBH in the bulge of the central galaxy, causing the quasar to light up. (ii) A random collision between satellites leads to a merger and a quasar episode if there is a burst of star formation. (iii) A quasar is still shining when its dark halo merges with a larger halo. The case (iii) hardly happens because of the short lifetime scale of quasar. Both the case (i) and the case (ii) can occur simultaneously. Thus, it is possible that a dark halo contains several quasars. On the other hand, since Kauffmann & Haehnelt (2000) did not consider the random collision, the case (ii) never happens in their model. Thus, in their model, a dark halo contains only one quasar at most. However, their model also reproduced well the observed relation between spheroid luminosity and black hole mass in nearby galaxies, and the evolution of the quasar luminosity functions. Therefore, in order to constrain our model for quasar formation, we will consider other properties of quasars in the next chapter.

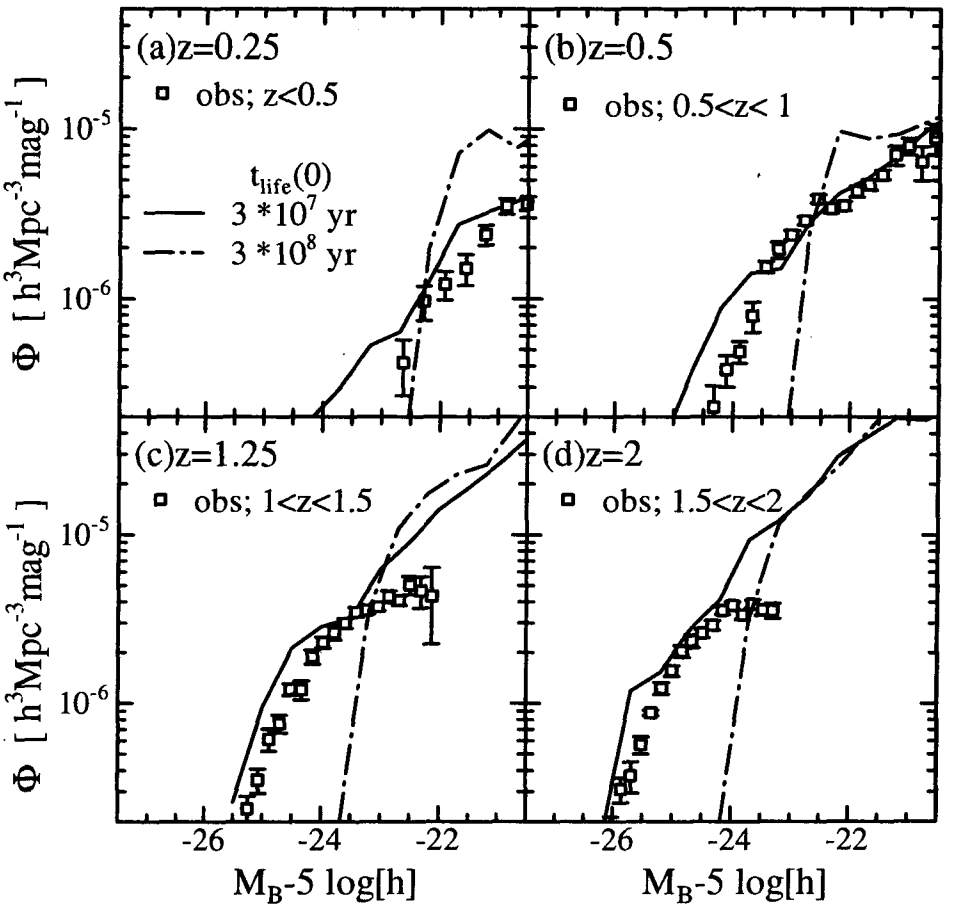

Figure 3.5: B-band quasar luminosity functions at (a)$z = 0.25$, (b) $z = 0.5$, (c)$z = 1.25$, and (d)$z = 2.0$. The solid lines are $t_{\rm life}(0) = 3 \times 10^7$yr and the dot-dashed lines are $t_{\rm life}(0) = 3 \times 10^8$yr. The symbols show the results from the 2dF 10k catalogue (Croom et al. (2001)) reanalyzed by Takeuchi for a cosmology $\Omega_0 = 0.3, \lambda_0 = 0.7$, and $h = 0.7$.

Chapter 4

Environment of Quasars

4.1 Introduction

Because of their very high intrinsic luminosities, quasars can be used as probe of the large-scale structure in high redshift universe. For more than three decades, we have known that quasars are associated with enhancements in the spatial distributions of galaxies (Bahcall, Schmidt & Gunn 1969). However, it is not obvious problem whether quasars trace underlying dark matter distribution or not. In this chapter, we investigate the environments of quasars using our model. We consider the halo mass dependence of the mean number of quasars in a dark halo, the effective bias parameter of quasar, and the probability distribution of the number of galaxies around quasars, as characterizations of the environments of quasars (Enoki, Nagashima & Gouda 2003). This is because the former two quantities are the measures of the relationship between quasars and dark matter distributions, and the latter provides the relationship between galaxies and quasars.

4.2 The halo mass dependence of the mean number of quasars in a dark halo

In this section, we consider the mean numbers of quasars and galaxies in a dark halo. We can compute these quantities directly from our model. In figure 4.1, we plot $\langle N_{\rm gal}(M)\rangle$ and $\langle N_{\rm QSO}(M)\rangle$, which denote the mean number of galaxies and quasars in a halo with mass, M, respectively, at (a) $z = 0.5$ and (b) $z = 2.0$. We select galaxies with $M_B - 5\log(h) < -19$ and quasars with $M_B - 5\log(h) < -21$, where M_B is the absolute B-band magnitude. It should be noted that changing the selection criteria of the magnitude for galaxies and quasars would alter these results, but qualitative features are not altered. As can be seen in figure 4.1, there are more galaxies and quasars at high z. At higher redshift, halos have more cold gas available to form stars and to fuel SMBHs because there has been relatively little time for star formation to deplete the cold gas at these redshifts. Thus, the number of luminous galaxies grows. Furthermore, at higher redshift, both the timescales of the dynamical friction and the random collisions are shorter because the mass density of a halo is higher. Therefore, the galaxy merging rate increases. Consequently, the number of

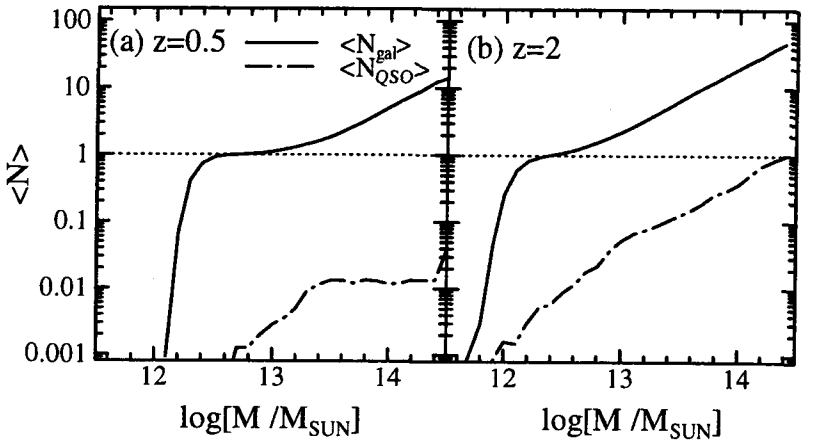

Figure 4.1: Mean numbers of galaxies with $M_B - 5\log(h) < -19$ (solid lines) and quasars with $M_B - 5\log(h) < -21$ (dot-dashed lines) in a dark halo with mass, M, at (a) $z = 0.5$ and (b) $z = 2.0$. The horizontal dotted line marks $\langle N_{\rm gal}\rangle = 1$ and $\langle N_{\rm QSO}\rangle = 1$

quasars also grows. Moreover, the decrease in the quasar lifetime, $t_{\rm life}$, with a redshift also contributes to the increase in the number of quasars because quasars become brighter as a result of the decrease in $t_{\rm life}$ (eq. [3.2.2]). From figure 4.1, we find that the dependence of $\langle N_{\rm QSO}(M)\rangle$ on halo mass, M, is different from the dependence of $\langle N_{\rm gal}(M)\rangle$. Furthermore, figure 4.2 shows that the ratio of $\langle N_{\rm QSO}(M)\rangle$ to $\langle N_{\rm gal}(M)\rangle$ varies with redshift and halo mass.

The mean numbers of quasars and galaxies in a dark halo provide the information of the relations among galaxies, quasars and dark halos. However, these quantities are not observable because it is very difficult to identify dark halos observationally. Then, using these quantities, we will calculate the *bias* parameter in the next section. The bias parameter is the ratio of galaxy or quasar density fluctuation to dark matter density fluctuation. Then, this quantity gives the relations the relation among quasar distribution, galaxy distribution and dark matter distribution. Furthermore, the bias parameter predicted by models can be compared with the one obtained by observation.

4.3 Quasar bias

The spatial distribution of dark matter need not be the same as the spatial distribution of quasars, galaxies and dark halos. In other words, the distributions of quasars, galaxies and dark halo may be biased realizations of the underlying dark matter density fluctuation, $\delta_{\rm DM}$. A simplified view of bias is that the two density fluctuation are simply proportional each other,

$$\delta_{\rm Q} = b_{\rm Q}\delta_{\rm DM}, \tag{4.3.1}$$
$$\delta_{\rm G} = b_{\rm G}\delta_{\rm DM}, \tag{4.3.2}$$
$$\delta_{\rm H} = b_{\rm H}\delta_{\rm DM}, \tag{4.3.3}$$

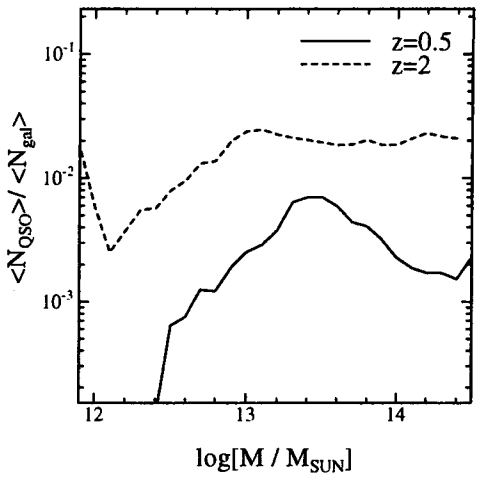

Figure 4.2: Ratio of the mean number of galaxies with $M_B - 5\log(h) < -19$ to the mean number of quasars with $M_B - 5\log(h) < -21$ in a dark halo with mass , M, at $z = 0.5$ (solid line) and $z = 2.0$ (dot-dashed line).

where $\delta_{\rm Q}$, $\delta_{\rm G}$ and $\delta_{\rm H}$ are the density fluctuations of quasars, galaxies and dark halos, respectively. Here, $b_{\rm Q}$, $b_{\rm G}$ and $b_{\rm H}$ are the linear bias parameters of quasars, galaxies and dark halos, respectively. In this case, the bias parameter of quasar is obtained by

$$b_{\rm Q}^2 = \frac{\xi_{\rm QQ}}{\xi_{\rm DM}}, \tag{4.3.4}$$

where $\xi_{\rm QQ}$ is the quasar two-point correlation function of and $\xi_{\rm DM}$ is the dark matter correlation function (see B.2.2). Once cosmological parameters are specified, we can obtain $\xi_{\rm DM}$ from a result of N-body simulation or an approximated fitting formula of e.g. Peacock & Dodds (1996). If $b_{\rm Q}$ is calculated by quasar formation model, we can obtain observable quantity $\xi_{\rm QQ}$. Therefore, here we calculate the bias parameter using our quasar formation model.

Generally, the quasar spatial distribution does not necessarily coincide with the galaxy spatial distribution. Benson et al. (2000) used a combination of cosmological N-body simulation and semi-analytic modeling of galaxy formation, and showed that the galaxy spatial distribution is sensitive to the efficiency with which galaxies form in halos with different mass. Seljak (2000) also obtained the same conclusion using an analytic model of galaxy clustering (see also Cooray & Sheth 2002). These results are applicable to the quasar spatial distribution. Therefore, our result in the previous subsection indicates that the clustering properties of galaxies are not the same as those of quasars, and that the bias in the spatial distribution of galaxies relative to that of dark matter is not the same as the bias in the spatial distribution of quasars.

One method for investigating the distributions of galaxies and quasars is to use a cosmological N-body simulation. Combing SAM for galaxy formation and cosmological N-body simulations certainly provides a powerful technique to investigate the galaxy distribution. However, since the number of quasar is a factor $10^3 \sim 10^4$ smaller than

the number of galaxy, it would be impossible to obtain a robust measurement of ξ_{QQ} from N-body simulations. Therefore, we use a simple analytic model to compute the bias parameter (Baugh et al 1999).

If we assume that the biases are independent of the scale, we can calculate the effective biases of objects (galaxies or quasars) using the method of Baugh et al (1999), as follows:

$$b_{\rm eff}(z) = \frac{\int b_{\rm H}(M,z)\langle N(M,z)\rangle n(M;z){\rm d}M}{\int \langle N(M,z)\rangle n(M;z){\rm d}M}, \tag{4.3.5}$$

where $b_{\rm H}(M,z)$ is the bias parameter for dark matter halos of mass, M, at z, $\langle N(M,z)\rangle$ denotes the mean number of objects (galaxies or quasars) that satisfy the selection criteria in a halo of mass, M, at z, and $n(M;z)$ is the dark halo mass function at z. This effective bias parameter is the mean of the bias of dark halos weighted by the number of objects in a dark halo and the number density of the dark halo. Note that these effective biases are valid for large scale ($\sim$ a few Mpc) where objects (galaxies or quasars) which contribute a two-point correlation function populate different halos.

Our SAM adopts the Press–Schechter mass function, which is given by

$$n(M;z)dM = \sqrt{\frac{2}{\pi}}\frac{\rho_0}{M}\frac{\delta_{\rm c}(z)}{\sigma^2(M)}\left|\frac{d\sigma(M)}{dM}\right|\exp\left[-\frac{1}{2}\frac{\delta_c^2(z)}{\sigma^2(M)}\right]dM, \tag{4.3.6}$$

where ρ_0 is the present mean density of the universe, $\sigma(M)$ is the rms linear density fluctuation on the scale M at $z = 0$ and $\delta_{\rm c}(z) = \delta_c/D(z)$. $D(z)$ is the linear growth factor, normalized to unity at the present day and δ_c is the linear critical density contrast at the collapse epoch (see Appendix B.3). Here, we use an approximate formula of δ_c for a spatially flat cosmological model (Nakamura & Suto 1997). The bias parameter for dark matter halos is given by Jing (1998),

$$b_{\rm H}(M,z) = \left\{1 + \frac{1}{\delta_c}\left[\frac{\delta_c^2(z)}{\sigma^2(M)} - 1\right]\right\}\left[\frac{\sigma^4(M)}{2\delta_c^4(z)} + 1\right]^{(0.06-0.02n_{\rm eff})}, \tag{4.3.7}$$

where $n_{\rm eff}$ is the effective spectral index of the power spectrum, ${\rm d}\ln P(k)/{\rm d}\ln k$, at the wavenumber defined by the Lagrangian radius of the dark matter halo, $k = 2\pi/r_L$ and $r_L = (3M/4\pi\rho_0)^{1/3}$ (see Appendix C.3). Figure 4.3 shows the evolution of effective bias for galaxies with $M_B - 5\log(h) < -19$ and quasars with $M_B - 5\log(h) < -21$. As can be seen in figure 4.3, quasars are higher biased tracers than galaxies. Furthermore, the evolution of quasar bias is different from that of galaxy bias. This is because that the dependence of $\langle N_{\rm QSO}(M,z)\rangle$ on the halo mass and the redshift is different from the dependence of $\langle N_{\rm gal}(M,z)\rangle$. The mean number of objects in a dark halo, $\langle N(M,z)\rangle$, is the increasing function with M. On the other hand, the mass function of dark halos, $n(M;z)$, is the decreasing function with M (see figure C.1). Therefore, $\langle N(M,z)\rangle n(M;z)$ has maximum at some halo mass, $M_{\rm p}$. Equation (4.3.5) indicates that the main contribution for $b_{\rm eff}(z)$ comes from the halo with mass $M_{\rm p}$. In our model, $M_{\rm p}$ for quasars is about $10^{13}M_\odot$ and $M_{\rm p}$ for galaxies is about $10^{12}M_\odot$. Thus, the bias parameters for quasars are larger than those for galaxies because the bias parameter for halos, $b_{\rm H}(M,z)$, is the increasing function with halo mass.

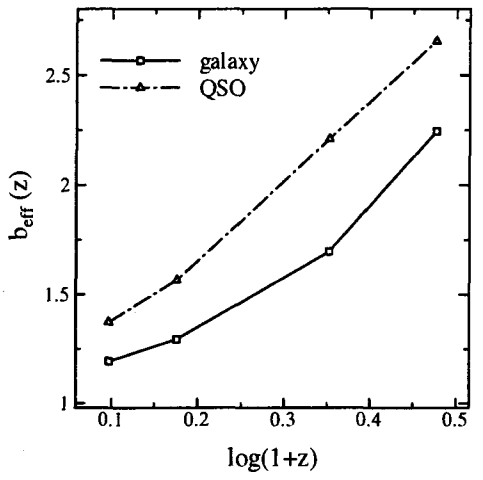

Figure 4.3: Effective bias parameter of galaxies with $M_B - 5\log(h) < -19$ (squares with solid line) and quasars with $M_B - 5\log(h) < -21$ (triangles with dot-dashed line) at $z = 0.25$, $z = 0.5$, $z = 1.25$, and $z = 2.0$.

4.4 The probability distribution of the number of galaxies around quasars

Next, we formulate the conditional probability that a halo with $N_{\rm QSO}$ quasars has $N_{\rm gal}$ galaxies. This provides the relationship between galaxies and quasars. The number density of the halos which contains $N_{\rm gal}$ galaxies and $N_{\rm QSO}$ quasars at z is obtained from the following expression:

$$n(N_{\rm gal}, N_{\rm QSO}; z) = \int N(N_{\rm gal}, N_{\rm QSO}|M; z)\, n(M; z) dM, \tag{4.4.1}$$

where $N(N_{\rm gal}, N_{\rm QSO}|M; z) dN_{\rm gal} dN_{\rm QSO}$ denotes the number of halos with mass M which contains $N_{\rm gal} \sim N_{\rm gal} + dN_{\rm gal}$ galaxies and $N_{\rm QSO} \sim N_{\rm QSO} + dN_{\rm QSO}$ quasars at z and $n(M; z)$ is the dark halo mass function at z. The number density of the halos which contain $N_{\rm QSO}$ quasars at z is obtained from:

$$n(N_{\rm QSO}; z) = \int N(N_{\rm QSO}|M; z) n(M; z) dM, \tag{4.4.2}$$

where $N(N_{\rm QSO}|M, z) dN_{\rm QSO}$ denotes the number of the halos with mass M which contain $N_{\rm QSO} \sim N_{\rm QSO} + dN_{\rm QSO}$ quasars at z. From equations (4.4.1) and (4.4.2), the conditional probability that the halo with $N_{\rm QSO}$ quasars has $N_{\rm gal} \sim N_{\rm gal} + dN_{\rm gal}$ galaxies at z is given by

$$P(N_{\rm gal}|N_{\rm QSO}; z) dN_{\rm gal} = \frac{n(N_{\rm gal}, N_{\rm QSO}; z)}{n(N_{\rm QSO}; z)} dN_{\rm gal}. \tag{4.4.3}$$

As can be seen in the above formulation, given $N(N_{\rm gal}, N_{\rm QSO}|M; z)$ and $N(N_{\rm QSO}|M; z)$ from the quasar formation model, one can calculate the probability distribution for the number of galaxies around quasars. Figure 4.4 shows these galaxy number distribution

functions around quasars estimated by our model. The results are shown for quasars brighter than $M_{\rm B} - 5\log(h) = -22$ and for galaxies brighter than $M_{\rm B} - 5\log(h) = -19$. Note that at $z = 0.25$ and $z = 0.5$ $P(N_{\rm gal}|N_{\rm QSO} = 2) = 0$ and $P(N_{\rm gal}|N_{\rm QSO} = 3) = 0$ for all $N_{\rm gal}$ (Fig. 4.4(a) and (b)) and that at $z = 1.25$ $P(N_{\rm gal}|N_{\rm QSO} = 3) = 0$ for all $N_{\rm gal}$ (Fig. 4.4(c)). At lower redshift, a halo has at most one quasar. Figures 4.4(a) and (b) show that the halo which has one quasar contains several galaxies by high probability. These results indicate that most quasars tend to reside in groups of galaxies at $0.2 \lesssim z \lesssim 0.5$, which consistent with the observation at $z \lesssim 0.4$ (e.g. Bahcall & Chokshi 1991; Fisher et al. 1996; McLure & Dunlop 2001). On the other hand, at higher redshift, the numbers of galaxies in the halo with one or two quasars is from several to dozens (Fig 4.4(c) and (d)). These results indicate that quasars locate over a range from small groups of galaxies to clusters of galaxies although most quasars locate in groups. Thus, at $1 \lesssim z \lesssim 2$ quasars seem to reside in more varied environments than at lower redshift. The results at higher redshift may be tested by statistics of galaxies around quasars which will be obtained in the future. In our model, we assume that quasar activity is triggered by galaxy major merger. From equation (2.4.1), the dynamical friction timescale is expressed as follows:

$$\tau_{\rm fric} \propto \frac{M_{\rm H}}{M_{\rm sat}} \frac{1}{\ln\left[1 + \left(\frac{M_{\rm H}}{M_{\rm sat}}\right)^2\right]}, \tag{4.4.4}$$

where $M_{\rm H}$ is the mass of dark halo, and $M_{\rm sat}$ is the mass of the satellite galaxy. This expression shows that $\tau_{\rm fric}$ increases with $M_{\rm H}/M_{\rm sat}$. Moreover, since collision timescale decreases with number of galaxies in a dark halo, but increases with the velocity dispersion of the dark halo, there will be a peak in the collision rate for a halo size about the mass of a group, $\sim 10^{13} M_{\odot}$. Furthermore, in our model, adopted quasar life timescale $t_{\rm life}$ is much shorter than the dynamical time scale of the dark halo where quasars and galaxies populate. Therefore, quasar activity reflects galaxy merger event directly. Thus, our model predicts that most quasars populate in groups.

The mean number of quasars per halo, $\langle N_{\rm QSO}(M)\rangle$, and probability distribution of the number of galaxies around quasars, $P(N_{\rm gal}|N_{\rm QSO})$, used in this study can provide some useful features of the quasar environments. Furthermore, the spatial quasar-galaxy correlation function is used in order to quantify the galaxy environments around a quasar because this quantity can be observed directly. Therefore, in order to constrain the quasar formation model more quantitatively, it is also necessary to predict spatial distribution of galaxies and quasars. We will show the results using the combination of cosmological N-body simulation and SAM for formation of galaxy and quasar in the next chapter.

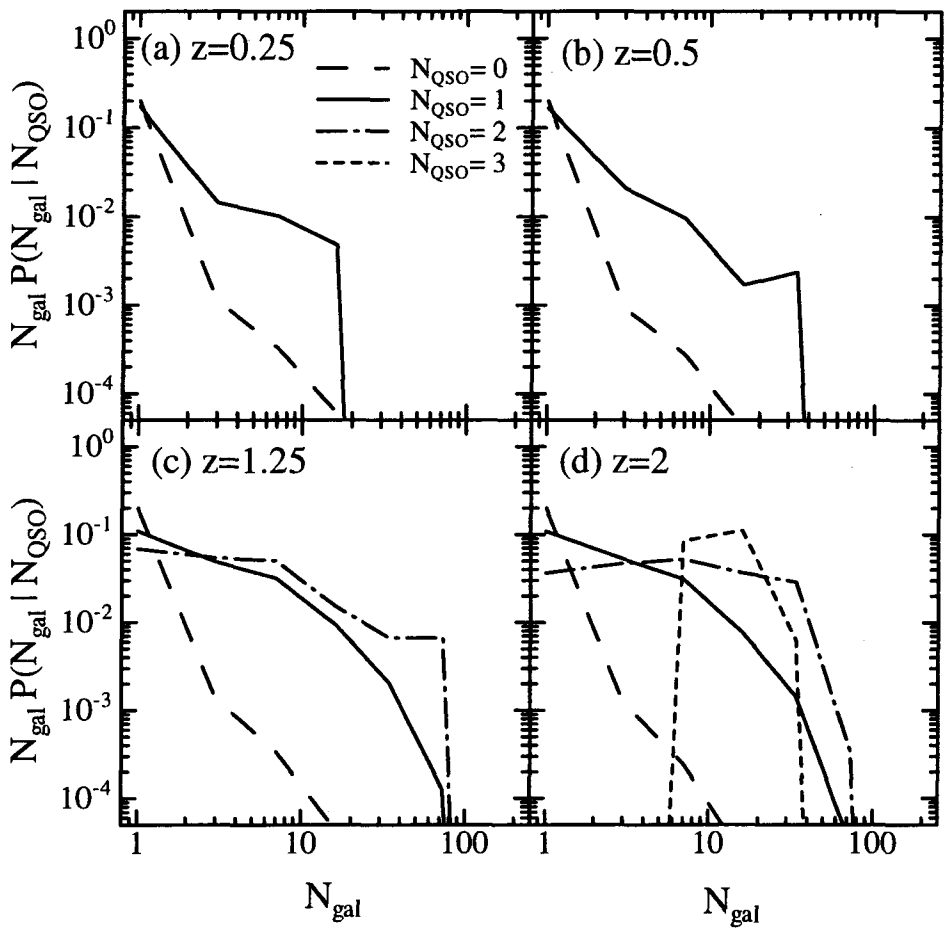

Figure 4.4: The probability distribution for the numbers of galaxies around quasars (a)$z = 0.25$, (b) $z = 0.5$, (c)$z = 1.25$ and (d)$z = 2.0$. The selected galaxies are brighter than $M_{\rm B} - 5\log(h) = -19$ and the selected quasars are brighter than $M_{\rm B} - 5\log(h) = -22$. Long-dashed, solid, dot-dashed and short-dashed lines show results for $N_{\rm QSO} = 0, 1, 2$ and 3 respectively.

Chapter 5

Clustering of Galaxies around Quasars

5.1 Incorporation with N-body simulation

In this chapter, we investigate the spatial cross-correlation between quasars and galaxies because this quantity can be observed directly. To do this, we must obtain spatial distributions of quasars and galaxies, especially on small scales (less than a few Mpc). Therefore, we combine our SAM of our galaxy and quasar formation, described in Chapter 2 and Chapter 3, with cosmological N-body simulations. In this study, we use a result of a cosmological N-body simulation given by Yahagi (2002), in which he adopted a scheme of adaptive mesh refinement (AMR). The simulation was carried out on the VPP5000 supercomputer installed at the National Astronomical Observatory, Japan. Our adopted cosmological model is a ΛCDM model with $\Omega_0 = 0.3, \lambda_0 = 0.7, \sigma_8 = 1.0$ and $h = 0.7$. The simulation contains 512^3 dark matter particles of mass about $10^8 M_\odot$ in a periodic box of $L = 70h^{-1}$ Mpc. The resolution of this simulation is now the highest among the cosmological N-body simulations in the world.

There are two approaches to combine SAMs with N-body simulations. In the first approach, the merger trees of dark halos are extracted directly from the N-body simulations (e.g. Roukema et al. 1997; Kauffmann et al. 1999; Okamoto & Nagashima 2001a, Okamoto & Nagashima 2001b). In the second approach, the mass and the spatial coordinates of each dark halo is extracted from the N-body simulation at the redshift of interest, and the merger tree of each dark halo is generated using the Monte Carlo method based on the extended Press-Schechter formalism (e.g. Kauffmann, Nusser, & Steinmetz 1997; Benson et al. 2000). In our study, we adopt the first way. One of the advantages of the first approach is that this approach circumvents any possible discrepancy between the extended Press-Schechter predictions and the merging histories in the N-body simulation.

The construction of merger trees from the simulation outputs involves the following steps. First, we obtain clusters of particles at each time step using the friends-of-friends method (FoF). FoF connects pairs of particles whose separation is smaller than the predefined linking length. We adopt the linking length that is 0.2 times the mean interparticle separation. Only clusters containing at least 10 particles ($\sim 10^9 M_\odot$) are defined as dark

halos. Next, we search the offspring halo of a dark halo. Not all particles in a dark halo at some time step may belong to one halo in the next time step. Thus, the offspring of a dark halo is defined as the halo containing the most of particles in the progenitor halo. This procedure repeats until the redshift of interest.

Then, we identify the positions of galaxies as follows: We assume that the position of the central galaxy of a halo is identical with that of its *marker particle* which is the most gravitationally bound particle in the dark halo. When several dark halos have merged, the properties of the central galaxy in the most massive progenitor of the halo are transferred to the central galaxy of the offspring halo. The central galaxies of less massive progenitors become satellite galaxies. The marker particles of satellite galaxies then remain fixed. Since the mergers of galaxies due to the dynamical friction or the random collision cannot be followed by this simulation, we use the galaxy merger criteria described in §2.4. After a merger of galaxies, the marker particle of the lager galaxy becomes the marker particle of the merged galaxy. More detailed description of construction of merger trees is in Yahagi et al. (2003).

The mass functions and merger trees of dark halos derived using the extended Press-Schechter formalism differ from those found in the simulation, although the difference of the mass functions is only a factor of a few in the number of halos. In figure 5.1, we show the mass functions obtained by the simulation and the mass functions of Press-Schechter. These differences affect galaxy formation histories, especially for faint galaxies. Therefore, we reset galaxy formation model parameters to reproduce local observations. For example, since the low mass dark halo abundances decrease in the N-body simulation, the strength of feedback should be deduced. It should be necessary to investigate in more detail about the effect of the difference of merger trees on the formation of galaxies and quasars as future work. Moreover, in this study, we also change the timescale of star formation for simplicity as follows,

$$\tau_* = \tau_*^0(1+\beta), \tag{5.1.1}$$

where β is the efficiency of reheating.

The newly adopted parameters of this SAM+N-body simulation are tabulated in table 5.1 and 5.2. In figure 5.2 we plot the results of local luminosity functions of galaxies represented by solid lines. Figure 5.3 shows the ratio of cold gas mass relative to B-band luminosity of spiral galaxies as a function of their luminosity. Figure 5.4 shows the black hole mass function in our model at $z = 0$. In figure 5.4, we plot the black hole mass function in our model at $z = 0$. The resultant luminosity functions of quasars at two different redshifts are shown in figure 5.5. The model shows a broad agreement with observations. Slight difference in the luminosity functions would disappear if we chose a parameter set more carefully, but the conclusions in this chapter do not significantly change by slightly changing the parameters.

Table 5.1: Galaxy Formation Model Parameters for SAM+N-body simulation

$V_{\rm hot}$ (km s^{-1})	$\alpha_{\rm hot}$	τ_*^0 (Gyr)	$f_{\rm merge}$	$f_{\rm bulge}$	R	y	Υ
80	4	2	1.8	0.5	5/3	0.038	1.5

Table 5.2: Quasar Model Parameters for SAM+N-body simulation

$f_{\rm BH}$	ϵ_B	$t_{\rm life}(0)$ (10^7yr)
0.012	0.0023	1.0

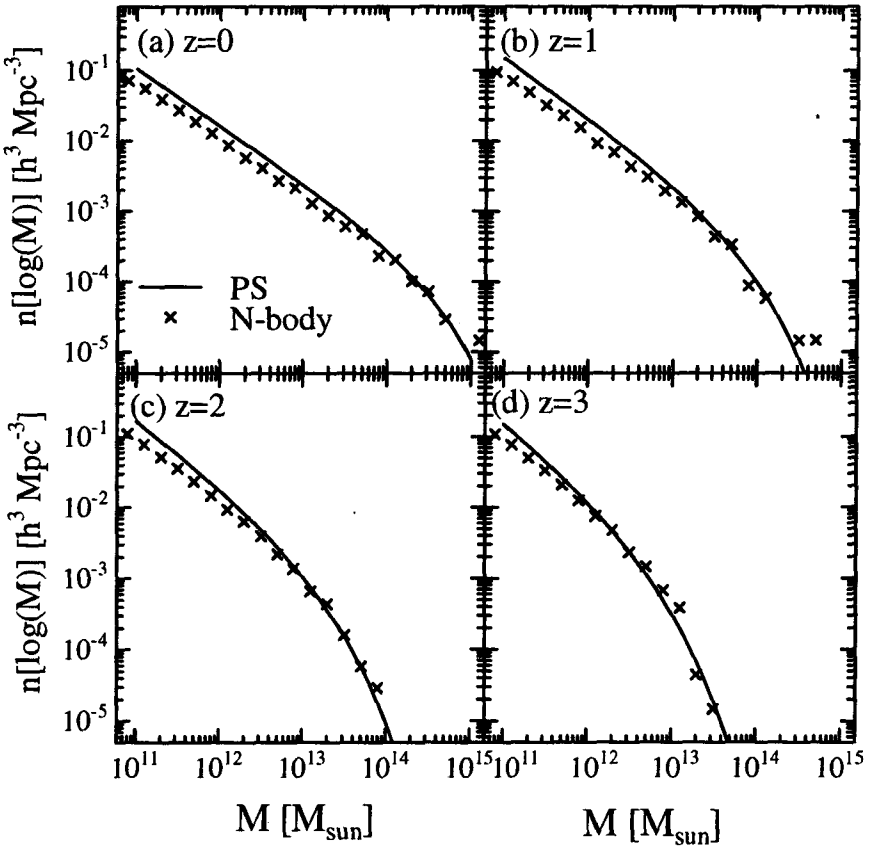

Figure 5.1: Mass functions of dark halos in the ΛCDM universe with $\Omega_0 = 0.3$, $\lambda_0 = 0.3$, $h = 0.7$, and $\sigma_8 = 1.0$, at (a)$z = 0$, (b) $z = 1$, (c)$z = 2$, and (d)$z = 3$. The solid lines are the Press-Schechter mass functions and the symbols are the mass functions obtained by the N-body simulation of Yahagi (2002).

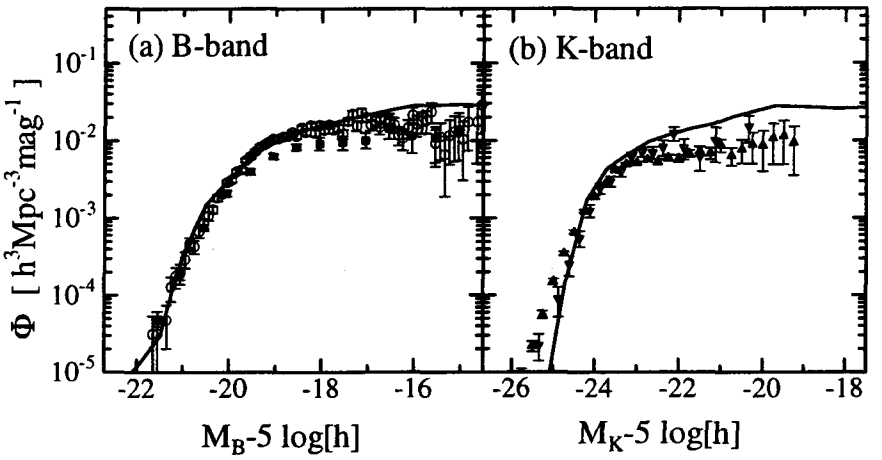

Figure 5.2: Local luminosity functions in the (a) B-band and (b) K-band. The thick lines show the results of the model of SAM+N-body simulation. The symbols with errorbars in (a) indicate the observational data from APM (Loveday et al. 1992, *filled squares*) and 2dF (Folkes et al. 1999, *open circles*). Symbols in (b) indicate the data from Gardner et al. (1997, *open inverted triangles*), and 2MASS (Cole et al. 2001, *filled triangles*).

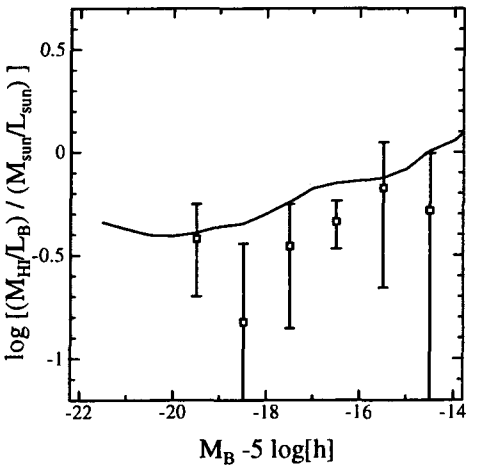

Figure 5.3: Cold gas mass relative to B-band luminosity of spiral galaxies. The thick line shows the result of the model of SAM+N-body simulation. The open squares with errorbars indicates the observational data for atomic hydrogen taken from Huchtmeier & Richter (1988). In the models, cold gas consists of all species of elements. Thus, we take $M_{\rm HI} = 0.75 M_{\rm cold}$, which corresponds to the fraction of hydrogen. Because the observational data denote only atomic hydrogen, they should be interpreted as lower limits of the ratio.

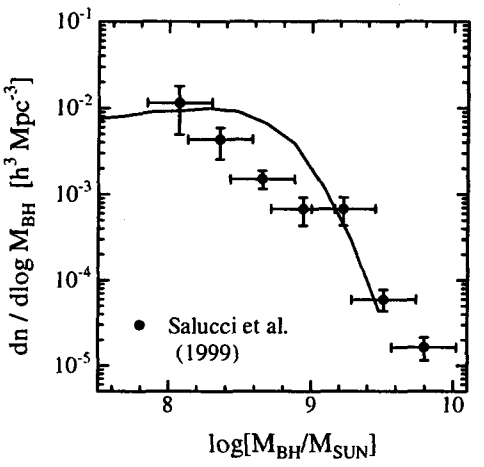

Figure 5.4: Black holes mass function of model at $z = 0$. The solid line indicates the model result of SAM+N-body simulation. The symbols with errorbars are the present black hole mass function obtained by Salucci et al. (1999).

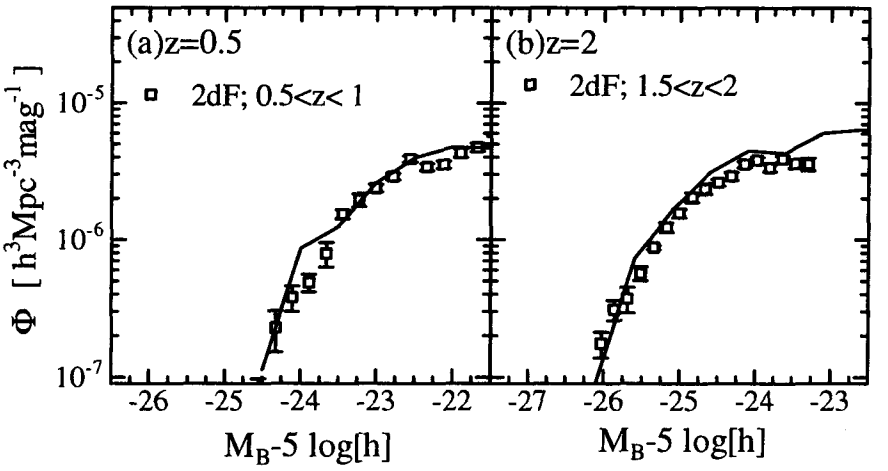

Figure 5.5: B-band quasar luminosity functions at (a)$z = 0.5$, and (b)$z = 2.0$. The solid lines show the results of SAM+N-body simulation. The symbols show results from the 2dF 10k catalogue (Croom et al. (2001)) reanalyzed by Takeuchi for a cosmology $\Omega_0 = 0.3, \lambda_0 = 0.7$, and $h = 0.7$.

5.2 Quasar-galaxy correlation

Figure 5.6 shows the distributions of quasars and galaxies in our simulation volume ($70^3\ h^{-3}$ Mpc^3) at $z = 1.24$. The dots show the galaxies with $M_B - 5\log(h) < -19$ and the circles show the quasars with $M_B - 5\log(h) < -20$, where M_B shows the absolute B-band magnitude. The resultant quasar-galaxy cross-correlation function ξ_{QG} does not much differ from the galaxy two-point correlation function ξ_{GG} (the cross-correlation and the two-point correlation are defined in B.2.2). Figure 5.7 shows ξ_{QG} and ξ_{GG} at $z = 2$, $z = 1.24$ and $z = 0.53$. The crosses show ξ_{QG} for quasars with $M_B - 5\log(h) < -20$ and for galaxies with $M_B - 5\log(h) < -19$. The open squares show ξ_{GG} for galaxies with $M_B - 5\log(h) < -19$. At each redshift, $\xi_{\rm QG}$ is about a factor of two larger than $\xi_{\rm GG}$ on small scale (about several hundreds kpc). On the other hand, $\xi_{\rm QG}$ is a similar to $\xi_{\rm GG}$ on large scale (more than a few Mpc). Therefore, these results show that quasars populate in a similar environment to the galaxies with $M_B - 5\log(h) < -19$ even in high redshift. In our model, we assume that the merger of galaxies triggers the quasar activity. Therefore, as is discussed in the previous chapter, our model predicts that most quasars populate in groups of galaxies because the galaxy merger rate has maximum in halos corresponding to groups of galaxies, $M \sim 10^{13} M_\odot$. The galaxies with $M_B - 5\log(h) < -19$ tend to populate in the halo with mass about several $10^{12} M_\odot$ (see figure 4.1). Thus, these results are qualitatively consistent with the conclusion of analysis for the galaxy number distribution function around quasars in the previous chapter, although the merger trees extracted from N-body simulations are different from the merger trees generated from extended Press–Schechter formalism. The selection criteria in magnitude for quasars, $M_B - 5\log(h) < -20$, is lower than usual criterion $M_B - 5\log(h) \lesssim -21$. This is because our simulation volume is so small that the number of sample quasar was too small if the latter criterion was adopted. Larger volume simulations are needed for more quantitative investigation of luminous quasar environment.

Kauffmann & Haehnelt (2002) also combined their SAM with cosmological N-body simulations and investigated the properties of ξ_{QG}. However, in their SAM, they assumed that the quasar is always located at the position of central galaxy in the halo because they do not consider the random collision of galaxies. Therefore, ξ_{QG} becomes large at small scale. In our model, since quasar activity is triggered by galaxy merger due to both dynamical friction and random collision, quasars do not always locate in the center of the halo. Thus, our results of ξ_{QG} on small scale are different from the results of Kauffmann & Haehnelt (2002). Therefore, comparing the model predictions about ξ_{QG} with observational results is a good test to constrain processes of galaxy merging and quasar formation scenarios.

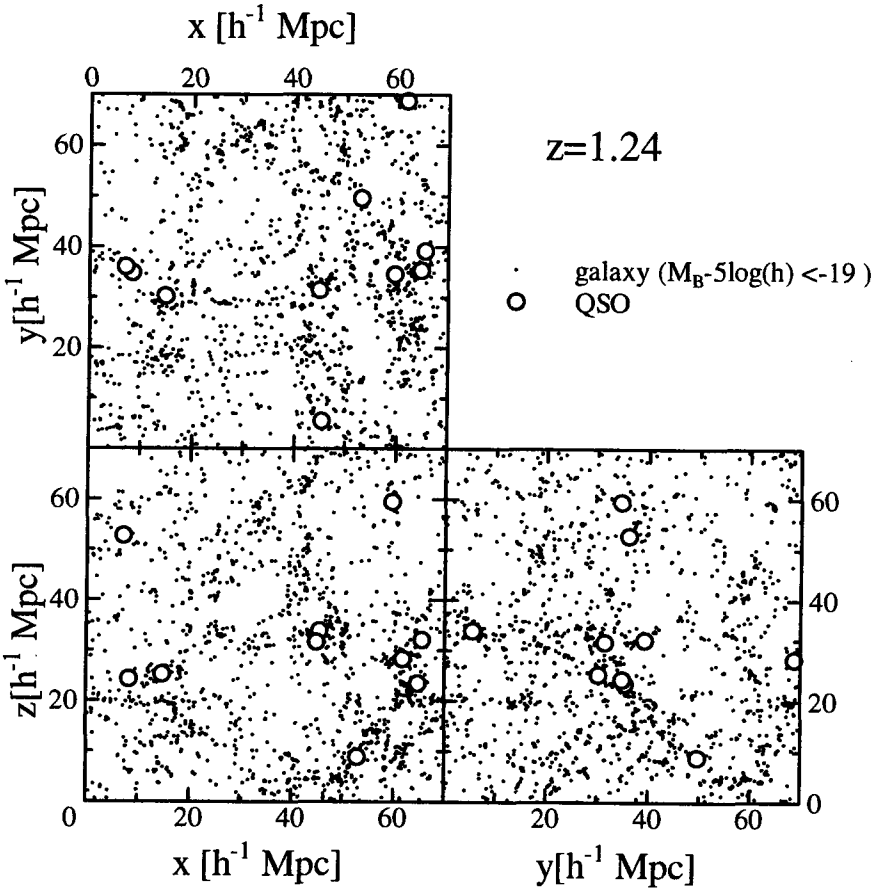

Figure 5.6: Spatial distributions of galaxies and quasar at $z = 1.24$ in the simulation box (70^3 h^{-3} Mpc^3). The dots show galaxies with $M_B - 5\log(h) < -19$. The circles show quasars with $M_B - 5\log(h) < -20$.

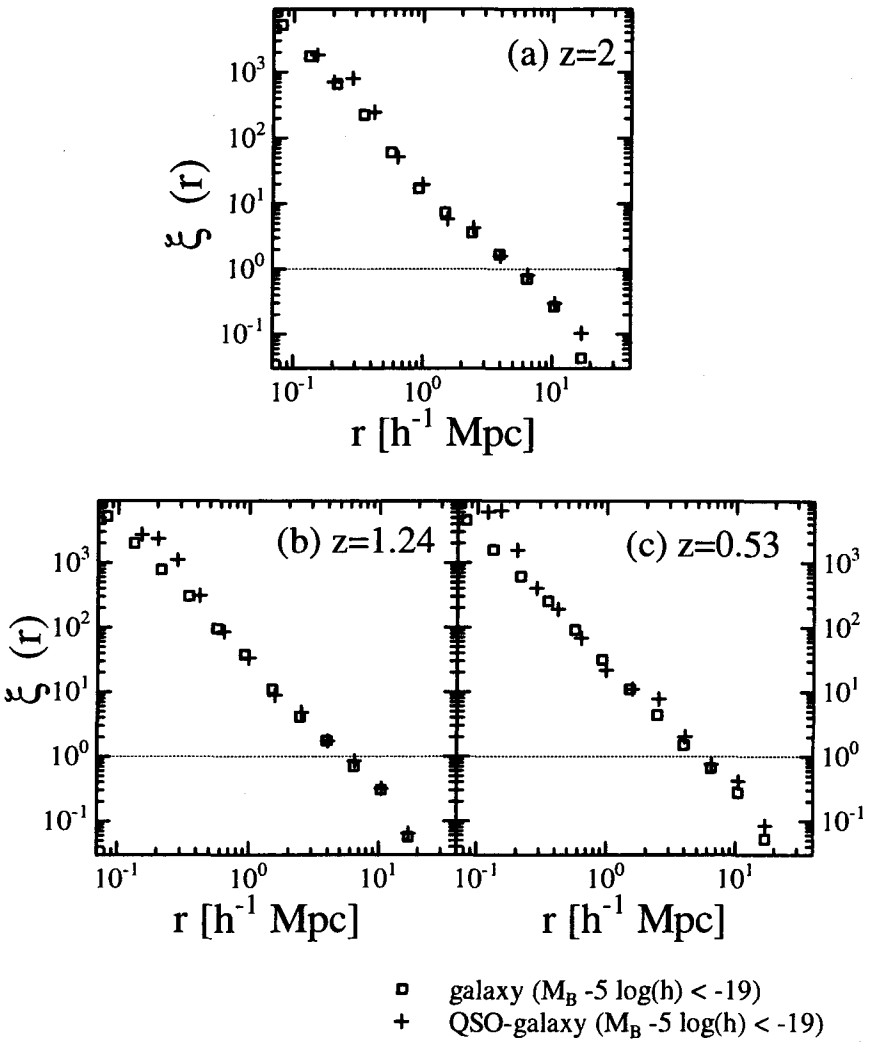

Figure 5.7: Evolution of quasar-galaxy cross-correlation functions and galaxy two-point correlation functions at three redshifts: $z = 2$ (a), $z = 1.24$ (b) and $z = 0.53$ (c). The crosses show quasar-galaxy cross-correlation function for quasars with $M_B - 5\log(h) < -20$ and for galaxies with $M_B - 5\log(h) < -19$. The open squares show galaxy two-point correlation functions for galaxies with $M_B - 5\log(h) < -19$. Horizontal lines mark $\xi(r) = 1$.

Chapter 6

Summary and Conclusion

We have constructed the unified semi-analytic model (SAM) for galaxy and quasar formation based on the hierarchical clustering scenario, and investigate environment of quasars using this model. First, we have predicted the mean number of quasars in a dark halo with mass M, $\langle N_{\rm QSO}(M)\rangle$, and the effective bias parameter of quasars $b_{\rm eff,QSO}(z)$ because they provide the relation between quasars and underlying mass distribution. Next, we have predicted probability distribution of the number of galaxies around quasars, $P(N_{\rm gal}|N_{\rm QSO})$, and quasar-galaxy cross-correlations, $\xi_{\rm QG}(r)$, because they provide the relationship between galaxies and quasars. These quantities reflect the processes of quasar formation such as the amount of cold gas available for fueling, the galaxy merger rate and the quasar lifetime. Therefore, by comparing these predictions with observations coming in the future, one will be able to constrain quasar formation models.

Our SAM for the galaxy formation can reproduce not only local observational results such as luminosity functions and the cold gas mass fraction in spiral galaxies, but also galaxy number counts and photometric redshift distribution of galaxies in the Hubble Deep Field (Chapter 2). Based on this galaxy formation model, we introduce a quasar formation model under the assumption that SMBHs are formed and fueled during major mergers of galaxies; the fueling process causes quasar activity. This model can reproduce not only the observed relation of the SMBH mass to spheroid luminosity, but also the quasar luminosity functions at different redshifts (Chapter 3). Using this model, we have investigated environmental characteristics of quasars (Chapter 4, Enoki, Nagashima & Gouda 2003).

First, we have shown $\langle N_{\rm QSO}(M)\rangle$ and $\langle N_{\rm gal}(M)\rangle$. We found that the dependence of $\langle N_{\rm QSO}(M)\rangle$ on halo mass M is different from the dependence of $\langle N_{\rm gal}(M)\rangle$. Moreover, we found that the ratio of $\langle N_{\rm QSO}(M)\rangle$ to $\langle N_{\rm gal}(M)\rangle$ varies with redshift and halo mass. The mean numbers of quasars and galaxies in a dark halo provide the relations among galaxies, quasars and dark halos. However, these quantities are not observable. Their behavior of them in our model suggests that the clustering of galaxies is not the same as the clustering of quasars. This is because the spatial distributions of galaxies and quasars are sensitive to the mean numbers of quasars and galaxies in a dark halo, and the mean number depends on the halo mass in a different way for galaxies and quasars. Therefore, we have calculated the effective bias parameter of quasars which is observable and we have shown that its evolution is different from that of galaxies. This reason is as follows. Both

the mean numbers of galaxies and quasars in a dark halo depend on the cold gas mass fraction in the halo. In our model, the major merger of galaxies leads to quasar activity, so the number of quasars strongly depends on the merger rate of galaxies. Therefore, the number of quasars in a dark halo is different from the number of galaxies in a dark halo.

Next, we have shown the galaxy number distribution function around quasars, $P(N_{\rm gal}|N_{\rm QSO})$. At lower redshifts ($0.2 \lesssim z \lesssim 0.5$), most halos that have quasars have at most several galaxies. This indicates that most quasars reside in groups of galaxies. On the other hand, at higher redshift ($1 \lesssim z \lesssim 2$), the number of galaxies in the halo with quasars is from several to dozens; quasars reside in ranging from small groups of galaxies to clusters of galaxies. These results show that most quasars at higher redshift reside in more various environments than at lower redshift. This model prediction at lower redshift is consistent with the observation at $z \lesssim 0.4$ (e.g. Bahcall & Chokshi 1991; Fisher et al. 1996; McLure & Dunlop 2001). The results at higher redshift are checkable by statistics of galaxies around quasars which will be obtained in the future. In our model, we assume that the major merger of galaxies triggers quasar activity. As is described in §2.4, the galaxy merger rate has maximum in dark halos corresponding to groups of galaxies, $M \sim 10^{13} M_{\odot}$. Therefore, our model predicts that most quasars populate in groups.

Finally, we have analyzed the spatial cross-correlation function between quasars and galaxies, $\xi_{\rm QG}$, and the galaxy two-point correlation function, $\xi_{\rm GG}$. To do this, we must obtain spatial distribution of quasars and galaxies, especially in small scale (less than a few Mpc). Therefore, we combine our SAM for galaxy and quasar formation with cosmological N-body simulation (Chapter 5). Comparison of quasar-galaxy cross correlation function with galaxy two-point correlation function shows that $\xi_{\rm QG}$ is a factor ~ 3 larger than $\xi_{\rm GG}$ on small scale (about several hundreds kpc). On the other hand, $\xi_{\rm QG}$ is a similar to $\xi_{\rm GG}$ on large scale (more than a few Mpc). The above predictions are also resulted from the fact that quasars tend to populate in groups of galaxies. Although the merger trees extracted from N-body simulations are slightly different from the merger trees generated from extended Press–Schechter formalism, this conclusion is consistent with the conclusion of analysis for the galaxy number distribution function around quasars. It should be necessary to investigate in detail about the effect of the difference of merger trees on galaxy and quasar formation as a future work. To do this, we need to quantify the difference between the merger trees extracted from N-body simulations and the merger trees obtained from extended Press–Schechter formalism.

Our predictions about the galaxy number distribution and quasar-galaxy cross correlation at low redshift are consistent with observations. The results of observations coming in the near future at high redshift will constrain our quasar formation model. The quasar bias parameter of our model results may be tested by forthcoming data from the 2dF quasar redshift survey (Croom et al. 2001) and the Sloan Digital Sky Survey (York et al. 2000). Moreover, since the SDSS will provide deep imaging of all of the quasar fields, it will be possible to study the relationship between quasars and their local environments for a large number of quasars. Comparing the observational results with our model prediction about the galaxy number distribution and quasar-galaxy cross correlation will enable us to constrain our quasar formation model.

It is still controversial whether the environments of quasars depend on their optical and radio luminosities. Some authors have claimed that radio-loud quasars were located

in richer environments than radio-quiet quasars at $z < 0.6$ (e.g. Yee & Green 1984; Yee & Green 1987; Ellingson, Yee & Green 1991; Hintzen, Romanishin & Vlades 1991). However, other people obtained different results. For example, Hutchings, Crampton & Johnson (1995) observed the galaxy environment of radio-loud quasars and radio-quiet quasars and concluded that there is no significant difference in the richness. Recent studies support this conclusion (e.g. Wold et al. 2001). The discrepancies between different studies may be caused partly by too small quasar samples and by differences in sample selection of quasars and galaxies. This situation will soon improve with the availability of a new generation of very large quasar surveys such as the 2dF quasar redshift survey and the SDSS. Although we do not deal with radio properties of quasars in this thesis, our investigation about quasar environments will also provide a clue for understanding the radio characteristics of quasars from their environments.

In this thesis, we fix the parameters in the model of galaxy formation, when we incorporated a quasar formation model and investigated properties of quasars. The parameters are determined by comparison with some observational results. However, since various physical processes are intricately involved in galaxy formation, there may be some parameters which can reproduce the observational results. Therefore, the parameters in the model may be changed by comparing with other new observational results which will be obtained in the future. Moreover, the model of galaxy formation will be improved as the understanding of each physical process in galaxy formation makes a progress. In our quasar model, the resultant properties of quasar depend on some properties of galaxy formation such as the amount of cold gas and the galaxy merger rate. Thus, change of the galaxy formation model may also lead to the change of the quasar formation model. Comparing with observational results which will be obtained in the future, and improving models of each physical process , we will be able to understand galaxy and quasar formation step by step. Our study would be a milestone for understanding problems of galaxy and quasar formation.

Acknowledgments

It is my great pleasure to thank my supervisor Fumio Takahara at Osaka University for continuous advice and encouragement. I am deeply grateful to my advisor Naoteru Gouda at National Astronomical Observatory of Japan (NAOJ), who led me to a research field of the galaxy formation, for proper guidance, continuous support and encouragement. Special thanks are also due to Masahiro Nagashima, who collaborates on this work, for proper advice, stimulating discussions and providing me with his numerical code for galaxy formation. I would also like to thank Hideki Yahagi, who collaborates on a part of this work, for stimulating discussions and providing me with data of his AMR cosmological simulations. I am also grateful to Misao Sasaki, Jun'Ichi Yokoyama, Satoshi Yoshioka, Haruhiko Ueda, and Katsuya Okoshi for discussions, useful comments and encouragement. I would also like to thanks Tsutomu T. Takeuchi for kindly providing me with the reanalyzed data of the quasar luminosity functions derived from the 2dF 10k catalogue. I am also thankful to members at Theoretical Astrophysics Group of Osaka University, and at Theoretical Astrophysics Division and Department of Fundamental Astrometry of NAOJ.

Finally, I am very grateful to my family for their continuous support and warm-hearted encouragement.

Appendix A

Background Cosmology

A.1 Homogeneous and isotropic universe

Our Universe is observed to be homogeneous and isotropic on scales much larger than about 100 Mpc. Therefore, in modern cosmology, it is widely accepted that the fundamental assumption is the global homogeneity and isotropy of our Universe. This idea is called *Cosmological Principle*. The spatially homogeneous and isotropic universe is described by a metric of the Robertson-Walker metric:

$$ds^2 = -c^2dt^2 + a(t)^2\left[\frac{dr^2}{1-Kr^2} + r^2(d\theta^2 + \sin^2\theta d\phi^2)\right], \tag{A.1.1}$$

where c is the speed of light, $a(t)$ is the scale factor, and K is the spatial curvature constant. The behavior of scale factor $a(t)$ is determined by the Einstein equation. Because of the homogeneity and isotropy, the energy-momentum tensor $T_{\mu\nu}$ has the same form as perfect fluid:

$$T^{\mu}_{\nu} = \mathrm{diag}(-\rho c^2, p, p, p), \tag{A.1.2}$$

where ρc^2 is the energy density and p is pressure. The Einstein equation reduces following equations:

$$\left(\frac{\dot{a}}{a}\right)^2 = \frac{8\pi G\rho}{3} - \frac{Kc^2}{a^2} + \frac{\Lambda c^2}{3}, \tag{A.1.3}$$

$$\dot{\rho}c^2 = -3\left(\frac{\dot{a}}{a}\right)\left(\rho c^2 + p\right), \tag{A.1.4}$$

where Λ is the cosmological constant and dots denote the time derivative, d/dt. These equations are Friedmann equations.

If an equation of state is $p = w\rho c^2$, equation (A.1.4) becomes $\rho \propto a^{-3(1+w)}$. For relativistic matter ($w = 1/3$) and non-relativistic matter ($w = 0$), we have

$$\rho = \rho_0 a^{-4} = \rho_0(1+z)^4 \ : \text{relativistic matter}, \tag{A.1.5}$$

$$\rho = \rho_0 a^{-3} = \rho_0(1+z)^3 \ : \text{non-relativistic matter}. \tag{A.1.6}$$

Here $z = a_0/a - 1$ is cosmological redshift, and a_0 is the present scale factor and we normalize $a_0 = 1$[1].

[1]Throughout appendixes, a scripts 0 denotes the present value, $z = 0$

Next, we define cosmological parameters as follows:

$$H \equiv \frac{\dot{a}}{a} \text{ : Hubble parameter,} \tag{A.1.7}$$

$$\Omega \equiv \frac{\rho(t)}{\rho_c(t)} = \frac{8\pi G\rho}{3H^2} \text{ : density parameter} \tag{A.1.8}$$

$$k \equiv \frac{Kc^2}{a^2H^2} \text{ : curvature parameter,} \tag{A.1.9}$$

$$\lambda \equiv \frac{\Lambda c^2}{3H^2} \text{ : normalized cosmological constant.} \tag{A.1.10}$$

Here $\rho_c \equiv 3H^2/8\pi G$ is called the critical density of the universe. The present critical density is $\rho_{c,0} = 3H_0^2/8\pi G = 1.9 \times 10^{-29} h^2 \mathrm{gcm}^{-3}$ where h is the dimensionless Hubble constant in units of 100 km s^{-1} Mpc^{-1}. Note that normalized cosmological constant λ is no longer a constant but varies with time. Using these cosmological parameters, equation (A.1.3) can rewritten as

$$\Omega(t) + \lambda(t) - k(t) = 1. \tag{A.1.11}$$

In this thesis, collisionless and non-relativistic dominated Universe is focused on. In this universe, cosmological parameters at z are described as follows:

$$\begin{aligned} \Omega(z) &= \frac{8\pi G\rho_0}{3H_0^2}\frac{a_0^3}{a^3}\frac{H_0^2}{H^2} \\ &= \Omega_0(1+z)^3\frac{H_0^2}{H^2}, \end{aligned} \tag{A.1.12}$$

$$\begin{aligned} k(z) &= \frac{Kc^2}{a_0^2H_0^2}\frac{a_0^2H_0^2}{a^2H^2} \\ &= k_0(1+z)^2\frac{H_0^2}{H^2} \end{aligned} \tag{A.1.13}$$

$$\begin{aligned} \lambda(z) &= \frac{\Lambda c^2}{3H_0^2}\frac{H_0^2}{H^2}, \\ &= \lambda_0\frac{H_0^2}{H^2}. \end{aligned} \tag{A.1.14}$$

From equation (A.1.11)-(A.1.14), one obtains the dynamical equation of the universe:

$$\begin{aligned} \frac{H^2}{H_0^2} &= \frac{\Omega_0}{a^3} + \frac{1-\Omega_0-\lambda_0}{a^2} + \lambda_0 \\ &= \{\Omega_0(1+z)^3 + (1-\Omega_0-\lambda_0)(1+z)^2 + \lambda_0\}, \end{aligned} \tag{A.1.15}$$

and the evolution of the density parameter:

$$\Omega(z) = \frac{\Omega_0(1+z)^3}{\Omega_0(1+z)^3 + (1-\Omega_0-\lambda_0)(1+z)^2 + \lambda_0}. \tag{A.1.16}$$

A.2 Solutions of Friedmann equation

We show the exact solutions in some representative cases in following three cosmological models.

(i) Einstein-de Sitter Universe : $\Omega_0 = 1,\ k_0 = \lambda_0 = 0$
From (A.1.3), we have

$$a = \left(\frac{3}{2}H_0 t\right)^{2/3}. \tag{A.2.1}$$

From (A.1.15), the Hubble parameter is given by

$$\frac{H^2}{H_0^2} = (1+z)^3, \tag{A.2.2}$$

and from (A.1.16), the density parameter is given by

$$\Omega(z) = \Omega_0 = 1. \tag{A.2.3}$$

(ii) Open Universe : $\Omega_0 < 1,\ \lambda_0 = 0,\ k_0 = \Omega_0 - 1 < 0$
In this case, note that $-c^2K = a^2H^2(1-\Omega) = a_0^2H_0^2(1-\Omega_0)$. From (A.1.3), we obtain the parametric solution of a and t as follows:

$$a = \frac{\Omega_0}{2(1-\Omega_0)}(\cosh\eta - 1), \tag{A.2.4}$$

$$H_0 t = \frac{\Omega_0}{2(1-\Omega_0)^{3/2}}(\sinh\eta - \eta). \tag{A.2.5}$$

From (A.1.15), the Hubble parameter is given by

$$\begin{aligned}\frac{H^2}{H_0^2} &= \Omega_0(1+z)^3 + (1-\Omega_0)(1+z)^2 \\ &= (1+\Omega_0 z)(1+z)^2,\end{aligned} \tag{A.2.6}$$

and from (A.1.16), the density parameter is given by

$$\Omega(z) = \frac{\Omega_0(1+z)^3}{\Omega_0(1+z)^3 + (1-\Omega_0)(1+z)^2} = \frac{\Omega_0(1+z)}{1+\Omega_0 z}. \tag{A.2.7}$$

Next, we derive the relation between t and z. From (A.2.4), we obtain

$$\cosh\eta = 2X + 1, \tag{A.2.8}$$

$$\sinh\eta = 2X^{1/2}(1+X)^{1/2}, \tag{A.2.9}$$

Here, we define the variable X as

$$X \equiv \frac{1}{\Omega(z)} - 1 = \left(\frac{1}{\Omega_0} - 1\right)\frac{1}{1+z}. \tag{A.2.10}$$

Then, we obtain

$$\eta = 2\ln\left[X^{1/2} + (1+X)^{1/2}\right]. \tag{A.2.11}$$

From these equations and (A.2.5), the relation between t and z is given by

$$H_0 t = \frac{\Omega_0}{1-\Omega_0}\left\{X^{1/2}(1+X)^{1/2} + \ln\left[X^{1/2} + (1+X)^{1/2}\right]\right\}. \tag{A.2.12}$$

(iii) Spatially Flat Universe : $k_0 = 0,\ \Omega_0 < 1,\ \Omega_0 + \lambda_0 = 1$
From (A.1.3), we obtain

$$a = \left(\frac{\Omega_0}{1-\Omega_0}\right)^{1/3} \sinh^{2/3}\left(\frac{3}{2}\sqrt{1-\Omega_0}H_0 t\right). \tag{A.2.13}$$

From (A.1.15), the Hubble parameter is given by

$$\frac{H^2}{H_0^2} = \Omega_0(1+z)^3 + \lambda_0 = \Omega_0(1+z)^3 + 1 - \Omega_0 \tag{A.2.14}$$

and from (A.1.16), the density parameter is given by

$$\Omega(z) = \frac{\Omega_0(1+z)^3}{\Omega_0(1+z)^3 + \lambda_0} = \frac{\Omega_0(1+z)^3}{\Omega_0(1+z)^3 + 1 - \Omega_0}. \tag{A.2.15}$$

From (A.2.13), the relation between t and z is given by

$$H_0 t = \frac{2}{3\sqrt{1-\Omega_0}} \ln\left[X^{1/2} + \left(1 + X^{1/2}\right)\right]. \tag{A.2.16}$$

Here, we define the variable X as

$$X \equiv \frac{1}{\Omega(z)} - 1 = \left(\frac{1}{\Omega_0} - 1\right)\frac{1}{(1+z)^3}, \tag{A.2.17}$$

and we use $\sinh^{-1} x = \ln(x + \sqrt{x^2+1})$.

Appendix B

Inhomogeneous Universe

In this section, we summarize the gravitational evolution of density fluctuations after non-relativistic matter dominates in the universe. Since, the fluctuation scale which we interested in is much smaller than the horizon scale of the universe, Newtonian gravity is a good approximation.

B.1 Linear perturbation theory

The proper separation of two points varies with time as

$$\mathbf{r} = a(t)\mathbf{x}, \tag{B.1.1}$$

where $\mathbf{r}$ is the physical coordinate and $\mathbf{x}$ is expanding coordinate comoving with background universe. This yields the relations for velocity as follows:

$$\dot{\mathbf{r}} = \dot{a}\mathbf{x} + a\dot{\mathbf{x}} = H\mathbf{r} + \mathbf{v}(\mathbf{x}, \mathbf{t}), \tag{B.1.2}$$

where the first term on the right hand side is the global uniform expansion and the second term is the peculiar velocity. For non-relativistic ideal fluid, the evolution equations of density fluctuation are continuity equation, Euler equation of motion and Poisson equation of gravitational field (e.g. Peebles 1980) are describe as follows:

$$\frac{\partial \delta}{\partial t} + \frac{1}{a}\nabla \cdot [(1+\delta)\mathbf{v}] = 0, \tag{B.1.3}$$

$$\frac{\partial \mathbf{v}}{\partial t} + H\mathbf{v} + \frac{1}{a}(\mathbf{v}\cdot\nabla)\mathbf{v} = -\frac{\nabla p}{\rho a} - \frac{1}{a}\nabla\phi, \tag{B.1.4}$$

$$\nabla^2\phi = 4\pi\rho_b a^2 \delta. \tag{B.1.5}$$

where ∇ is the derivative with respect to $\mathbf{x}$, and p and ϕ are respectively the perturbed pressure and gravitational potential. The density contrast δ and its Fourier decomposition are defined by

$$\delta(\mathbf{x}, t) \equiv \frac{\rho(\mathbf{x}, t) - \rho_b(t)}{\rho_b(t)} \tag{B.1.6}$$

$$= \frac{1}{(2\pi)^3}\int \delta_{\mathbf{k}}(t)\exp(i\mathbf{k}\cdot\mathbf{x})d^3\mathbf{k} \tag{B.1.7}$$

where $\rho_b(t)$ is the mean density of background universe, which simply by ρ in the previous section. $\rho(\mathbf{x}, t)$ means the local density at $\mathbf{x}$ and t.

If the perturbed quantities are small enough, above equations are linearized. Taking the Fourier decomposition of density contrast, the evolution of density contrast is describe as:

$$\ddot{\delta}_{\mathbf{k}} + 2H\dot{\delta}_{\mathbf{k}} = \left(4\pi G\rho_b - \frac{c_s^2 k^2}{a^2}\right)\delta_{\mathbf{k}}, \tag{B.1.8}$$

where $c_s \equiv \sqrt{\partial p/\partial \rho}$ is the sound speed, and $k = |\mathbf{k}|$. In the equation (B.1.8), the first term on the right hand side denotes the destabilizing effect of gravity and the second term denotes the stabilizing effect of gas pressure. On small scales (corresponding to large k), pressure dominates and density contrast does not grow and oscillate. On the other hand, on the large scales (corresponding to small k),, gravity dominates and density contrast grow monotonically. The border between these two regimes is presented by the Jeans wave number defined by

$$k_{\mathrm{J}}^2 \equiv \frac{4\pi G\rho_b a^2}{C_s^2}. \tag{B.1.9}$$

For $k \ll k_{\mathrm{J}}$, the solution of equation (B.1.8) can be written as

$$\delta_{\mathbf{k}}(t) = A(\mathbf{k})D_+(t) + B(\mathbf{k})D_-(t). \tag{B.1.10}$$

The growing mode D_+ and decaying mode D_- are given in term of scale factor by

$$D_+ \propto H(a)\int^a \frac{d\acute{a}}{H(\acute{a})}d\acute{a} \tag{B.1.11}$$

$$D_- \propto H(a) \tag{B.1.12}$$

where $H(a)$ is the Hubble parameter at $z = 1/a - 1$. We consider only the growing mode and neglect decaying mode. The expressions for this growing mode $D(t)$ for three cosmological models mentioned in A.2 are:

(i) Einstein-de Sitter universe : $\Omega_0 = 1,\ k_0 = \lambda_0 = 0$

$$D(t) = a(t)D(t_0) \tag{B.1.13}$$

(ii) Open universe : $\Omega_0 < 1,\ k_0 > 0,\ \lambda_0 = 0$

$$D(t) \propto \frac{3\sinh\eta\ (\sinh\eta - \eta)}{(\cosh\eta - 1)^2} - 2 \tag{B.1.14}$$

(iii) Flat model with positive Λ : $\Omega_0 + \lambda_0 = 1,\ k_0 = 0$

$$D(t) \propto \sqrt{1 + \frac{1}{X^3}}\int_0^y du\left(\frac{u}{2+u^3}\right)^{\frac{2}{3}} \tag{B.1.15}$$

where X is defined by $X \equiv (\Omega_0^{-1} - 1)^{\frac{1}{3}}a(t)$.

For spatially flat universe, the approximative expression is known as follows (Carroll, Press & Turner 1992):

$$D(t) = a(t)\frac{g(\Omega)}{g(\Omega_0)}D(t_0) \tag{B.1.16}$$

where $g(\Omega)$ is a growth suppression factor given by

$$g(\Omega) \equiv \frac{5}{2}\Omega\left[\frac{1}{70} + \frac{209}{140}\Omega - \frac{\Omega^2}{140} + \Omega^{\frac{4}{7}}\right]^{-1}. \tag{B.1.17}$$

and Ω is

$$\Omega = \frac{\Omega_0(1+z)^3}{\Omega_0(1+z)^3 + 1 - \Omega_0}. \tag{B.1.18}$$

B.2 Statistics of density fluctuation

B.2.1 Power spectrum

In this subsection, we describe statistics of density fluctuations. Let us Fourier expand $\delta(\mathbf{x}, t)$ as

$$\delta(\mathbf{x}, t) = \frac{1}{(2\pi)^3}\int \delta_{\mathbf{k}}(t)\exp(i\mathbf{k}\cdot\mathbf{x})d^3\mathbf{k}, \tag{B.2.1}$$

$$\delta_{\mathbf{k}}(t) = \int \delta(\mathbf{x}, t)\exp(-i\mathbf{k}\cdot\mathbf{x})d^3\mathbf{x}, \tag{B.2.2}$$

and define the power spectrum $P(\mathbf{k}, t)$ as

$$P(\mathbf{k}, t) = \langle|\delta_{\mathbf{k}}(t)|^2\rangle. \tag{B.2.3}$$

From the isotropy and homogeneity of the universe, power spectrum does not depend a preferred direction: $P(\mathbf{k}) = P(k)$. It is generally assumed that the primordial density field is random Gaussian. The Gaussian density field is completely characterized by its power spectrum, $P(k)$. For lack of any better assumptions, it is usually assumed that the primordial power spectrum of mass density fluctuation was a simple power-law

$$P_i(k) \propto k^{n_i} \tag{B.2.4}$$

where n_i is the initial spectral index. The growth of density fluctuations is affected several physical processes and the power spectrum is altered from its primordial spectral shape. The processed power spectrum is then given by

$$P(k) = P_i(k)T^2(k), \tag{B.2.5}$$

where $T(k)$ is a transfer function which represents the changes in the primordial spectral shape.

Next, we define a density fluctuations that is averaged over a volume V containing mass $M = \rho_b V$ as

$$\begin{aligned} \delta(M, \mathbf{x}, t) &= \int_V \delta(\mathbf{y}, t) W_M(|\mathbf{x} - \mathbf{y}|) d^3\mathbf{y} \\ &= \frac{1}{(2\pi)^3} \int \delta_{\mathbf{k}}(t) \hat{W}_M(k) \exp(i\mathbf{k} \cdot \mathbf{x}) d^3\mathbf{k}, \end{aligned} \tag{B.2.6}$$

where $W_M(r)$ is window function and $\hat{W}_M(k)$ is the Fourier components of $W_M(r)$. One example of the window function is a top-hat form:

$$W_M(r) = \begin{cases} 3/(4\pi R^3) & r < R \\ 0 & r > R, \end{cases} \tag{B.2.7}$$

$$\hat{W}_M(k) = \frac{3}{(kR)^3} \{\sin(kR) - kR\cos(kR)\}, \tag{B.2.8}$$

where $R \equiv (3M/4\pi\rho_b)^{1/3}$ is the filtering length. Then, the variance of the smoothed density fluctuation over the mass scale M at t is given by

$$\begin{aligned} \sigma^2(M, t) &\equiv \langle |\delta(M, \mathbf{x}, t)|^2 \rangle \\ &= \frac{1}{(2\pi)^3} \int P(k, t) \hat{W}_M^2(k) d^3\mathbf{k}. \end{aligned} \tag{B.2.9}$$

In this thesis, we adopt the power spectrum of mass density fluctuation in the CDM universe and assume $n_{\rm i} = 1$. The power spectrum in the CDM universe is well described by fitting formula of Bardeen et al. (1986):

$$P(k) = AkT^2(k), \tag{B.2.10}$$

$$T(k) = \frac{\ln(1 + 2.34q)}{2.34q} \left[1 + 3.89q + (16.1q)^2 + (5.46q)^3 + (6.71q)^4\right]^{-1/4}, \tag{B.2.11}$$

where A is the proportional constant and $q \equiv k/(\Gamma h \ \mathrm{Mpc}^{-1})$. Here, Γ is the shape parameter given by Sugiyama (1995)

$$\Gamma \equiv \Omega_0 h \exp\left[-\Omega_{\rm b}\left(1 + \sqrt{2h}\,\Omega_0^{-1}\right)\right], \tag{B.2.12}$$

where $\Omega_{\rm b}$ is baryonic density parameter. Effects of baryon density on the CDM transfer functions have been included by this shape parameter. In this study, the amplitude of power spectrum, the proportional constant A in (B.2.10), is fixed by the present variance of the smoothed density fluctuation over the scale $R = 8h^{-1}$Mpc:

$$\sigma_8 \equiv \sigma(R = 8h^{-1}\mathrm{Mpc}, t_0). \tag{B.2.13}$$

B.2.2 Two-point correlation function

The two-point correlation function is defined as the joint ensemble average of the density fluctuation at two different points,

$$\xi(r) \equiv \langle \delta(\mathbf{x})\delta(\mathbf{x}+\mathbf{r}) \rangle, \tag{B.2.14}$$

which depends only on $r = |\mathbf{r}|$ due to the isotropy and homogeneity of the universe. The two-point correlation function is the Fourier transform of the power spectrum as follows

$$\xi(r) = \frac{1}{(2\pi)^3} \int P(k) \exp(i\mathbf{k}\cdot\mathbf{x}) d^3\mathbf{k}. \tag{B.2.15}$$

The physical interpretation of $\xi(r)$ is that it measures the excess probability for finding two particles at volume element dV_1 and dV_2 that are separated by distance $r = |x_1 - x_2|$,

$$dP_{12}(r) = \bar{n}^2[1 + \xi(r)]dV_1 dV_2 \tag{B.2.16}$$

where $\bar{n}$ is the mean density. Since the probability of finding a particle in dV_1 is $\bar{n}dV_1$, the conditional probability that there is a particle at dV_2 given that there is one at dV_1 is

$$dP(2|1) = \bar{n}[1 + \xi(r)]dV_2. \tag{B.2.17}$$

A related quantity is the cross-correlation function. Here, one considers two different classes of objects (A and B, say), and the cross-correlation function $\xi_{AB}(r)$ is defined as the probability for finding for a object A at volume element dV_1 and a object B at dV_2 that are separated by distance r,

$$dP_{AB}(r) = \bar{n}_A \bar{n}_B [1 + \xi_{AB}(r)]dV_1 dV_2, \tag{B.2.18}$$

where $\bar{n}_A$ and $\bar{n}_B$ are the mean densities of objects A and B, respectively.

B.3 Spherical collapse model

B.3.1 Evolution of spherical overdense region

As density contrast grows and becomes nearly unity, the linear perturbation theory described in §B.1 fails. It is reasonable to expect that overdense regions will break away from background expansion, collapse and form gravitationally bound objects like galaxies or clusters of galaxies. Generally, it is very difficult to fully trace non-liner evolution analytically. However, for the case of spherically symmetric perturbations, one can obtain exact solutions (Tomita 1969; Gunn & Gott 1972).

Suppose the motion of spherical mass shell with radius r. We assume the shell crossing does not occur, the equation of motion for the mass shell is then

$$\ddot{r} = -\frac{GM}{r^2}, \tag{B.3.1}$$

where $M = M(< r)$ is the mass enclosed within the radius r. Integrating this equations gives

$$\frac{1}{2}\dot{r}^2 - \frac{GM}{r} = E, \tag{B.3.2}$$

where E is a constant of integration. In the case of $E < 0$, the mass shell collapses and a parametric form solution of equation (B.3.2) is given by

$$r = \frac{GM}{C}(1 - \cos\theta), \tag{B.3.3}$$

$$t = \frac{GM}{C^{3/2}}(\theta - \sin\theta), \tag{B.3.4}$$

where $C = -E/2$ and it is assumed that $r = 0$ at $t = 0$. At an early epoch ($\theta \ll 1$), above solutions are expanded as a series in θ:

$$r = \frac{GM}{2C}\left(\frac{t}{t_c}\right)\left[1 - \frac{1}{20}\left(\frac{t}{t_c}\right)^{2/3}\right], \tag{B.3.5}$$

$$t = t_c\,\theta^3\left(1 - \frac{\theta^2}{20}\right), \tag{B.3.6}$$

where $t_c \equiv GM/6C^{3/2}$. In this case, the mean density within the mass shell, $\rho(t)$, is given by

$$\rho(t) \simeq \frac{1}{6\pi G t^2}\left[1 + \frac{3}{20}\left(\frac{t}{t_c}\right)^{2/3}\right]. \tag{B.3.7}$$

In an Einstein-de Sitter universe, the mean density varies as $\rho_b(t) = 1/(6\pi G t^2)$, therefore, density contrast is described by

$$\delta(M,t) = \frac{\rho(t) - \rho_b(t)}{\rho_b(t)} = \frac{3}{20}\left(\frac{t}{t_c}\right)^{2/3} \propto D(t), \tag{B.3.8}$$

where $D(t)$ is the linear growth factor in §B.1.

Equations (B.3.3) and (B.3.4) imply that the mass shell will reach a maximum radius $r_{\rm max}$ at $\theta = \pi$, then contract and finally collapse to a point at $\theta = 2\pi$. In reality, shell crossing will occur and reach virial equilibrium by a process known as violent relaxation. The time at which the system reaches the equilibrium, $t_{\rm vir}$, is assumed to be at $\theta = 2\pi$. The radius of the virialized objects is obtained by the virial theorem:

$$r_{\rm vir} = \frac{r_{\rm max}}{2} = \frac{GM}{C}, \tag{B.3.9}$$

and the mean density of the objects, $\rho_{\rm vir}$, is given by

$$\rho_{\rm vir} = \frac{3C^3}{4\pi G^3 M^2}. \tag{B.3.10}$$

The ratio of $\rho_{\rm vir}$ to the critical density of the universe $\rho_c(t_{\rm vir})$ at this epoch is defined by

$$\begin{aligned}\Delta_c &\equiv \frac{\rho_{\rm vir}}{\rho_c(t_{\rm vir})} \\ &= \frac{\rho_{\rm vir}}{\rho_b(t_{\rm vir})}\Omega(t_{\rm vir}) \\ &= \frac{\rho_{\rm vir}}{\rho_{c,0}(1+z_{\rm vir})^3}\frac{\Omega(z_{\rm vir})}{\Omega_0}.\end{aligned} \tag{B.3.11}$$

where $z_{\rm vir}$ is the redshift corresponding to $t_{\rm vir}$. For convenience, the linear density contrast extrapolated to this epoch, $\delta_c \equiv \delta_{\rm lin}(t_{\rm vir})$, is considered. If the density contrast of a region predicted by linear theory reaches this value, δ_c, the region is thought to have collapsed at that time. For some specific cosmologies, Δ_c and δ_c are obtained in the following.

(i) Einstein-de Sitter universe : $\Omega_0 = 1,\ k_0 = \lambda_0 = 0$

$$\begin{aligned} \Delta_c &= 18\pi^2 \simeq 178 \\ \delta_c &= \frac{3(12\pi)^{2/3}}{20} \simeq 1.69 \end{aligned} \tag{B.3.12}$$

(ii) Open universe : $\Omega_0 < 1,\ k_0 > 0,\ \lambda_0 = 0$

$$\begin{aligned} \Delta_c &= 4\pi^2\, \Omega(t_{\rm vir}) \frac{(\cosh\eta_{\rm vir} - 1)^3}{(\sinh\eta_{\rm vir} - \eta_{\rm vir})^2} \\ \delta_c &= \frac{3}{2}\left[\frac{3\sinh\eta_{\rm vir}(\sinh\eta_{\rm vir} - \eta_{\rm vir})}{(\cosh\eta_{\rm vir} - 1)^2} - 2\right]\left[1 + \left(\frac{2\pi}{\sinh\eta_{\rm vir} - \eta_{\rm vir}}\right)^{2/3}\right] \end{aligned} \tag{B.3.13}$$

(iii) Flat model with positive Λ : $\Omega_0 + \lambda_0 = 1,\ k_0 = 0$

$$\begin{aligned} \Delta_c &= \Omega(t_{\rm vir})\left(\frac{r_{\rm max}}{r_{\rm vir}}\right)^3 \frac{2w_{\rm vir}}{\chi} \\ \delta_c &\simeq \frac{3(12\pi)^{2/3}}{20}(1 + 0.0123\log\Omega(t_{\rm vir})) \end{aligned} \tag{B.3.14}$$

where $w_{\rm vir} \equiv 1/\Omega(t_{\rm vir}) - 1$, and $\chi \equiv \lambda_0 H_0^2 r_{\rm max}^3/(GM)$.

Equation (B.3.13) is derived by Lacey & Cole (1993), and equation (B.3.14) is derived by Nakamura & Suto (1997). In practice, we use fitting formula of Bryan & Norman (1998) for virial density:

$$\begin{aligned} \Delta_c &= 18\pi^2 + 60x - 32x^2 \quad \text{for } \lambda_0 = 0 \\ \Delta_c &= 18\pi^2 + 82x - 39x^2 \quad \text{for } k_0 = 0 \end{aligned} \tag{B.3.15}$$

where $x \equiv \Omega(t_{\rm vir}) - 1$. This formula is accurate to 1 % in the range $0.1 \lesssim \Omega \lesssim 1$.

B.3.2 Properties of virialized object

Consider the virialized object with mass M formed at $z_{\rm vir}$. The virial radius of the object is defined as

$$\begin{aligned} R_{\rm vir} &\equiv \left(\frac{3M}{4\pi\rho_{\rm vir}}\right)^{1/3} \\ &= \left(\frac{3M}{4\pi\rho_{c,0}\Delta_{\rm vir}}\right)^{1/3}, \end{aligned} \tag{B.3.16}$$

where $\Delta_{\rm vir} \equiv \rho_{\rm vir}/\rho_{\rm c,0} = (1+z_{\rm vir})^3\Delta_{\rm c}\Omega_0/\Omega(z_{\rm vir})$. The circular velocity of the object is defined as

$$\begin{aligned} V_{\rm circ} &\equiv \left(\frac{GM}{R_{\rm vir}}\right)^{1/2} \\ &= R_{\rm vir}\left(\frac{4\pi\rho_{\rm c,0}\Delta_{\rm vir}}{3}\right)^{1/2} \\ &= R_{\rm vir}H_0\left(\frac{\Delta_{\rm vir}}{2}\right)^{1/2} \\ &= 70.7\left(\frac{R_{\rm vir}}{h^{-1}{\rm Mpc}}\right)\Delta_{\rm vir}^{1/2}\ {\rm km\ s^{-1}}. \end{aligned} \tag{B.3.17}$$

Using $V_{\rm circ}$, the mass of the virialized object, M, is written as

$$\begin{aligned} M &= V_{\rm circ}^3\left(\frac{3}{4\pi\rho_{\rm vir}}\right)^{-1/2} \\ &= 3.26\times10^6\left(\frac{V_{\rm circ}}{1{\rm km\ s^{-1}}}\right)^3\Delta_{\rm vir}^{-1/2}\,h^{-1}\ M_\odot, \end{aligned} \tag{B.3.18}$$

and the virial radius, $r_{\rm vir}$, is written as

$$\begin{aligned} R_{\rm vir} &= \frac{GM}{V_{\rm circ}} \\ &= 4.35\times10^5\left(\frac{M}{10^{14}M_\odot}\right)\left(\frac{V_{\rm circ}}{1{\rm km\ s^{-1}}}\right)^{-2}\ {\rm Mpc}. \end{aligned} \tag{B.3.19}$$

The dynamical time of the virialized object, $\tau_{\rm dyn} \equiv R_{\rm vir}/V_{\rm circ}$, is given by

$$\begin{aligned} H_0\tau_{\rm dyn} &= \frac{H_0R_{\rm vir}}{V_{\rm circ}} \\ &= \left(\frac{\Delta_{\rm vir}}{2}\right)^{-1/2}. \end{aligned} \tag{B.3.20}$$

Appendix C

Extended Press-Schechter Formalism

Press & Schechter (1974) derived the number density of dark halos as a function of their mass (mass function). Although this mass function shows reasonably good agreements with mass function from N-body simulation, the original derivation provided by Press & Schechter (1974) is very heuristic and has many theoretical uncertainties (e.g. Monaco 1998). Bower (1991), Bond et al. (1991) and Lacey & Cole (1993) developed an alternative derivation of Press & Schechter (1974) mass function and extended the formalism in order to make calculations of merger tree. This approach is based on the spherical collapse model which is described in B.3 and the assumptions that the initial density field is random Gaussian and that variance of density fluctuations smoothed over the mass scale M, $\sigma^2(M)$, is monotonically decreasing function of M.

C.1 Mass function of dark halos

Consider an initial density field $\delta(\mathbf{x}, M)$ at some point $\mathbf{x}$ that is smoothed on mass scale M and is extrapolated to the present epoch t_0 using linear perturbation theory. As $M \to 0$, $\sigma^2(M) = \langle|\delta^2|\rangle \to 0$ and so $\delta(\mathbf{x}, M)$ approach zero. Here, $\sigma(M)$ is the rms linear density fluctuation on the scale M extrapolated to the present epoch t_0. As the smoothing scale M is decreased from infinity (or increases $\sigma(M)$ from 0), $\delta(\mathbf{x}, M)$ begins to wander away from zero and perform trajectory on $\sigma^2 - \delta$ plane. The trajectory followed by $\delta(\mathbf{x}, M)$ as $\sigma(M)$ increases is determined by the $\delta_{\mathbf{k}}$ values. For the most choice of window function, the smoothed density field contains correlations between various scales of M. However, if one use the sharp-k-space filtering, a simple analytic description can be obtained. This sharp-k-space filtering window function is defined as

$$\hat{W}_M(k) = \begin{cases} 1 & k < k_s(M) \\ 0 & k > k_s(M) \end{cases}, \tag{C.1.1}$$

where $k_s(M)$ is the cut off wave number corresponding to a mass scale M. In this case, since the various Fourier modes are uncorrelated as we assume Gaussian random field, the increment to $\delta(\mathbf{x}, M)$ when one increases $\sigma^2(M)$ is totally uncorrelated with previous step. The smoothed field $\delta(\mathbf{x}, M)$ executes a random walk as the smoothing scale is changed.

Therefore, the trajectory of $\delta(\mathbf{x}, M)$ is described by the diffusion equation:

$$\frac{\partial Q}{\partial \sigma^2} = \frac{1}{2}\frac{\partial^2 Q}{\partial \delta^2} \tag{C.1.2}$$

where $Q(\sigma^2, \delta)d\delta$ is the probability of a point in the universe having density contrast in the range δ to $\delta + d\delta$ at σ^2.

As described in §B.3, when the density contrast of a region predicted by linear theory $\delta_{lin}(t) \propto D(t)$ reaches δ_c at time t, the region is thought to have collapsed and virialized at that time. The linear density contrast of this region extrapolated to the present is

$$\delta_c(t) = \delta_c \frac{D(t_0)}{D(t)}. \tag{C.1.3}$$

Now suppose that at some $\sigma^2(M)$ a trajectory of $\delta(\mathbf{x}, M)$ exceeds a critical value $\delta_c(t)$ for the first time. In this case, we consider that the point $\mathbf{x}$ is part of an collapsed object of mass M at time t. Note that the point $\mathbf{x}$ does not belong to any lager mass than M since $\delta(\mathbf{x}, M)$ has not exceeded $\delta_c(t)$ at any lager mass than M.

To calculate the fraction of trajectories of δ that upcross the threshold $\delta_c(t)$ first is identical to solving equation (C.1.2) with boundary condition that exists an absorbing barrier at $\delta = \delta_c(t)$. The solution is given by Chandrasekhar (1943) as follows

$$Q\left[\sigma^2, \delta, \delta_c(t)\right] = \frac{1}{\sqrt{2\pi\sigma^2}}\left\{\exp\left(-\frac{\delta^2}{2\sigma^2}\right) - \exp\left[-\frac{(\delta - 2\delta_c(t))^2}{2\sigma^2}\right]\right\}. \tag{C.1.4}$$

Then the probability that a trajectory exceeds $\delta_c(t)$ first at $\sigma^2 \sim \sigma^2 + d\sigma^2$, $P[\sigma^2, \delta_c(t)]d\sigma^2$, is calculated as

$$\begin{aligned} P[\sigma^2, \delta_c(t)] &= -\frac{\partial}{\partial \sigma^2}\int_{-\infty}^{\delta_c(t)} Q(\sigma^2, \delta, \delta_c(t))d\delta \\ &= -\left[\frac{1}{2}\frac{\partial Q}{\partial \delta}\right]_{-\infty}^{\delta_c(t)} \\ &= \frac{1}{\sqrt{2\pi}}\frac{\delta_c(t)}{\sigma^3(M)}\exp\left[-\frac{\delta_c^2(t)}{2\sigma^2(M)}\right]. \end{aligned} \tag{C.1.5}$$

This expression indicates the fraction of mass associated with collapsed object with mass corresponding to $\sigma^2(M)$ at time t. Thus, the comoving number density of collapsed objects with mass $M \sim M + dM$ at time t is described as

$$\begin{aligned} n(M;t)dM &= \frac{\rho_0}{M}P[\sigma^2, \delta_c(t)]\left|\frac{d\sigma^2(M)}{dM}\right|dM \\ &= \sqrt{\frac{2}{\pi}}\frac{\rho_0}{M}\frac{\delta_c(t)}{\sigma^2(M)}\left|\frac{d\sigma(M)}{dM}\right|\exp\left[-\frac{1}{2}\frac{\delta_c^2(t)}{\sigma^2(M)}\right]dM, \end{aligned} \tag{C.1.6}$$

where ρ_0 is the present mean density of the universe. This is well-known expression for Press-Schechter mass function.

In figure C.1, we plot the Press-Schechter mass functions in the ΛCDM universe with $\Omega_0 = 0.3$, $\lambda_0 = 0.3$, $h = 0.7$, and $\sigma_8 = 1.0$. The number density of virialized objects decreases with time at small masses, while it increases at large masses.

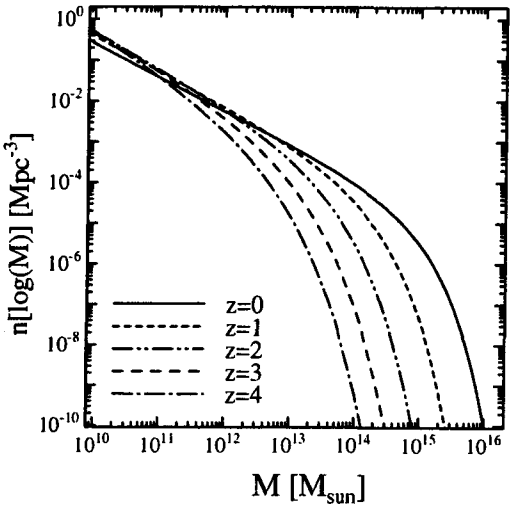

Figure C.1: The Press-Schechter mass functions in the ΛCDM universe with $\Omega_0 = 0.3$, $\lambda_0 = 0.3$, $h = 0.7$, and $\sigma_8 = 1.0$, at $z = 0$ (solid), $z = 1$ (short-dashed), $z = 2$ (dot-dot-dashed), $z = 3$ (dashed), and $z = 4$ (dot-dashed).

C.2 Progenitor halo mass distributions

The above derivation of mass function is readily extended to formulate the conditional probability that represents the fraction of mass in halos with mass M_2 at time t_2 that have merged to form halo with mass M_1 at time t_1 ($M_2 < M_1$, $t_2 < t_1$). This is the same problem as before. In this case, the starting point of trajectories of $\delta(\mathbf{x}, M)$ moves from the origin to the point at $(\sigma(M_1), t_1)$ on $\sigma^2 - \delta$ plane. This probability can be obtain by simply replacing $\sigma^2(M)$ with $\sigma^2(M_2) - \sigma^2(M_1)$ and $\delta_c(t)$ with $\delta_c(t_2) - \delta_c(t_1)$ in equation (C.1.5):

$$P(M_2, t_2|M_1, t_1)dM_2 = \frac{1}{\sqrt{2\pi}} \frac{\delta_{c2} - \delta_{c1}}{(\sigma_2^2 - \sigma_1^2)^{3/2}} \left|\frac{d\sigma_2^2}{dM_2}\right| \exp\left[-\frac{(\delta_{c2} - \delta_{c1})^2}{2(\sigma_2^2 - \sigma_1^2)}\right] dM_2 \qquad \text{(C.2.1)}$$

where $\sigma_i \equiv \sigma(M_i)$ and $\delta_{ci} \equiv \delta_c(t_i)$. Equation (C.2.1) yields the comoving number density of halos in the mass range $M_2 \sim M_2 + dM_2$ at time t_2 which are the progenitors of a halo with mass M_1 at time t_1 as follows,

$$n(M_2, t_2|M_1, t_1)dM_2 = \frac{M_1}{M_2} P_1(M_2, t_2|M_1, t_1)dM_2. \qquad \text{(C.2.2)}$$

This expression is derived by Lacey & Cole (1993).

C.3 Halo bias model

The clustering of dark halos is significantly different from that of the underlying dark matter. The ratio of the density fluctuation of dark halos to that of the underlying dark

matter is called *halo bias*. In this subsection, we review a simple model for halo bias, applying the mass distribution of progenitor halos described in the previous subsection.

Suppose we divide space up into cells of comoving volume V. The different cells may contain different amounts of mass M_1, which means they have different densities: $M_1/V = \rho_0(1+\delta)$. Let $N(M_2,t_2|M_1,t_1,V)dM_2$ denote the average number of $M_2 \sim M_2 + dM_2$ halos which collapsed at t_2, and are in cell size V which contains mass M_1 at t_1 ($M_2 < M_1$, $t_2 < t_1$). The overdensity of dark halos in such cell is

$$\delta_{\rm H}(M_2,t_2|M_1,t_1,V) = \frac{N(M_2,t_2|M_1,t_1,V)}{n(M_2,t_2)V} - 1. \tag{C.3.1}$$

Since a dark halo is a region which was sufficiently overdense that it collapsed, the number of halos within V equals the initial size of V times the number density of regions within it. The initial comoving size of V was $M_1/\rho_0 = V(1+\delta)$. Thus, we obtain $N(M_2,t_2|M_1,t_1,V) = n(M_2,t_2|M_1,t_1)V(1+\delta)$, where $n(M_2,t_2|M_1,t_1)$ is the comoving number density of progenitor halos derived in the previous subsection. The equation (C.3.1) becomes simple expression when $M_1 \gg M_2$ (so that $\sigma(M_1) \ll \sigma(M_2)$) and $|\delta_{c1}| \ll \delta_{c2}$ as follows (Mo & White 1996):

$$\delta_{\rm H}(M_2,t_2|M_1,t_1,V) \sim b_{\rm H}(M_2,t_2)\,\delta \tag{C.3.2}$$

where $b_{\rm H}(M,t)$ is the bias parameter of halo with mass M at t as follows:

$$b_{\rm H}(M,t) = 1 + \frac{1}{\delta_c}\left[\frac{\delta_c^2(t)}{\sigma^2(M)} - 1\right]. \tag{C.3.3}$$

Jing (1998) extended the comparison to higher resolution simulations and found that (C.3.3) underpredicts the bias of small halos with $M/M_* \ll 1$ where M_* is the characteristic mass defined by $\sigma(M_*) = \delta_{\rm c}(t)$. He obtained more accurate fitting formula with the slightly modified prescription:

$$b_{\rm H}(M,t) = \left\{1 + \frac{1}{\delta_c}\left[\frac{\delta_c^2(t)}{\sigma^2(M)} - 1\right]\right\}\left[\frac{\sigma^4(M)}{2\delta_c^4(t)} + 1\right]^{(0.06-0.02n_{\rm eff})}, \tag{C.3.4}$$

where $n_{\rm eff}$ is the effective spectral index of the power spectrum, $d\ln P(k)/d\ln k$, at the wavenumber defined by the Lagrangian radius of the dark matter halo, $k = 2\pi/r_L$ and $r_L = (3M/4\pi\rho_0)^{1/3}$. This formula is good approximation for $M \gtrsim 10^{-3}M_*$. Note that $b_{\rm H}(M,t)$ is the increasing function with M and the decreasing function with t. In figure C.1, we plot the halo bias, $b_{\rm H}(M,z)$, given by Jing (1998) in the ΛCDM universe with $\Omega_0 = 0.3$, $\lambda_0 = 0.3$, $h = 0.7$, and $\sigma_8 = 1.0$. In this case, $M_* \sim 10^{14}M_\odot$

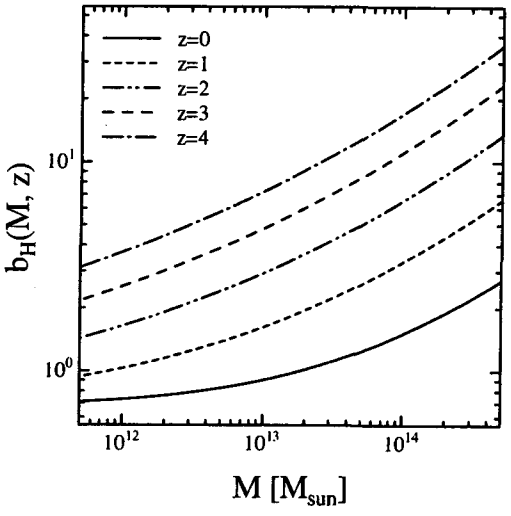

Figure C.2: The halo bias, $b_{\rm H}(M, z)$, given by Jing (1998) in the ΛCDM universe with $\Omega_0 = 0.3$, $\lambda_0 = 0.3$, $h = 0.7$, and $\sigma_8 = 1.0$, at $z = 0$ (solid), $z = 1$ (short-dashed), $z = 2$ (dot-dot-dashed), $z = 3$ (dashed), and $z = 4$ (dot-dashed).

Bibliography

Bahcall, J. N., Schmidt, M., & Gunn, J. E. 1969, ApJL, 157, L77

Bahcall, J. N., Kirhakos, S., Saxe, D. H., & Schneider, D. P. 1997, ApJ, 479, 642

Bahcall, N. A., & Chokshi, A. 1991, ApJL, 380, L9

Bardeen, J. M., Bond, J. R., Kaiser, N., & Szalay, A. S. 1986, ApJ, 304, 15

Barnes, J. E. 1988, ApJ, 331, 699

Barnes, J. E., & Hernquist, L. 1996, ApJ, 471, 115

Baugh, C. M., Benson, A. J., Cole, S., Frenk, C. S. & Lacey, C. G. 1999, MNRAS, 305, L21

Bennett, C. L., Banday, A. J., Gorski, K. M., Hinshaw, G., Jackson, P., Keegstra, P., Kogut, A., Smoot, G. F., Wilkinson, D. T. and Wright, E. L. 1996, ApJ, 464, L1

Benson, A. J., Cole, S., Frenk, C. S., Baugh C. M., & Lacey, C. G. 2000, MNRAS, 311, 793

Binney, J., & Tremaine, S. 1987, Galactic Dynamics, Princeton Univ. Press, Princeton, NJ

Blumenthal, G., Faber, S., Primack, J., & Rees, M. J. 1984, Nature, 311, 517

Bond, J. R., Cole, S. , Efstathiou, G., & Kaiser, N. 1991, ApJ, 379, 440

Bower, R. J. 1991, MNRAS, 248, 332

Boyle, B. J., & Terlevich, R. J. 1998, MNRAS, 293, L49

Bryan, G. L., & Norman, M. L. 1998, ApJ, 495, 80

Carroll, S. M., Press, W. H., & Turner, E. L. 1992, ARA&A, 30, 499

Cattaneo, A. 2001, MNRAS, 324, 128

Cen R. & Ostriker J. P. , 2000, ApJ, 538, 83

Chandrasekhar,S. 1943, Rev. Mod. Phys., 15,1

Cole, S. 1991, ApJ, 367, 45

Cole, S., Aragon-Salamanca, A., Frenk, C. S., Navarro, J. F., & Zepf, S. E. 1994, MNRAS, 271, 781

Cole, S., Lacey, C. G., Baugh, C. M., & Frenk, C. S. 2000, MNRAS, 319, 168

Cole, S., Norberg, P., Baugh, C. M., Frenk, C. S., Bland-Hawthorn, J., Bridges, T., Cannon, R., Colless, M., et al. 2001, MNRAS, 326, 255

Cooray, A. & Sheth, R. 2002, Phys. Rep., 371, 1

Cristiani, S. & Vio, R. 1990, A&A, 227, 385

Croom S. M., & Shanks T., 1999, MNRAS, 313, 411

Croom, S. M., Smith, R. J., Boyle, B. J., Shanks, T., Loaring, N. S., Miller, L., & Lewis, I. J., 2001, MNRAS, 322, L29

de Bernardis, P., Ade, P. A. R., Bock, J. J., Bond, J. R., Borrill, J., Boscaleri, A., Coble, K., Contaldi, C. R., Crill, B. P., De Troia, G., et al., 2002, ApJ, 564, 559

Diaferio, A., Kauffmann, G., Balogh, M. L., White, S. D. M., Schade, D., & Ellingson, E., 2001, MNRAS, 323, 999

Efstathiou, G., Ellis, R. S., & Peterson, B. A. 1988, MNRAS, 232, 431

Efstathiou, G. & Rees, M. J., 1988, MNRAS, 230, P5

Ellingson, E., Yee H. K. C., & Green, R. F., 1991, ApJ, 371, 49

Enoki, M., Nagashima, M., & Gouda, N., 2003, PASJ, 55, in press

Fisher, K. B., Bahcall, J. N., Kirhakos, S., & Schneider, D. P., 1996, ApJ, 468, 469

Folkes, S., Ronen, S., Price, I., Lahav, O., Colless, M., Maddox, S., Deeley, K., Glazebrook, K., et al. 1999, MNRAS, 308, 459

Franceschini, A., Hasinger, G., Miyaji, T., & Malquori, D. 1999, MNRAS, 310, L5

Freedman, W. L., Madore, B. F., Gibson, B. K., Ferrarese, L., Kelson, D. D., Sakai, S., Mould, J. R., Kennicutt, R. C. Jr., Ford, H. C., Graham, J. A., et al., 2001, ApJ, 553, 47

Gardner, J. P., Sharples, R. M., Frenk, C. S., & Carrasco, B. E. 1997, ApJL, 480, L99

Gebhardt, K., Bender, R., Bower, G., Dressler, A., Faber, S. M., Filippenko, A. V., Green, R., Grillmair, C., et al., 2000, ApJL, 539, L13

Gunn, J. E. & Gott, J. R. I. 1972, ApJ, 176, 1

Haehnelt, M., & Rees, M. J., 1993, MNRAS, 263, 168

Haehnelt, M., Natarajan, P. & Rees, M. J., 1998, MNRAS, 300, 817

Haiman, Z., & Loeb, A., 1998, ApJ, 503, 505

Hernquist, L. 1992, ApJ, 400, 460

Hernquist, L. 1993, ApJ, 409, 548

Heyl, J.S., Hernquist, L., & Spergel, D. 1994, ApJ, 427, 165

Hintzen, P., Romanishin, W., & Valdes, F., 1991, ApJ, 366, 7

Hosokawa, T., Mineshige, S., Kawaguchi, T., Yoshikawa, K., & Umemura, M. 2001, PASJ, 53, 861

Hutchings, J. B., Crampton, D., & Johnson, A., 1995, AJ, 109, 73

Huchtmeier, W. K., & Richter, O. -G. 1988, A&A, 203, 237

Jing, Y.P., 1998, ApJ 503, L9

Kauffmann, G., & White, S.D.M., 1993, MNRAS, 261, 921

Kauffmann, G., White, S.D.M. & Guiderdoni, 1993, MNRAS, 264, 201

Kauffmann, G., Nusser, A., & Steinmetz M., 1997, MNRAS, 311, 795

Kauffmann, G., & Charlot, S., 1998, MNRAS, 297, 23

Kauffmann, G., Colberg, J. M., Diaferio, A., & White, S. D. M., 1999, MNRAS, 311, 188

Kauffmann, G., & Haehnelt, M. 2000, MNRAS, 311, 576

Kauffmann, G., & Haehnelt, M. 2002, MNRAS, 332, 529

Kodama, T., & Arimoto, N. 1997, A&A, 320, 41

Kormendy, J., & Richstone, D., 1995, ARA&A, 33, 581

Lacey, C. G., & Cole, S. 1993, MNRAS, 262, 627

Loveday, J., Peterson, B. A., Efstathiou, G., & Maddox, S. J. 1992, ApJ, 90, 338

Lynden-Bell, D. 1969, Nature , 223, 690

Magorrian, J., Tremaine, S., Richstone, D., Bender, R., Bower, G., Dressler, A., Faber, S. M., Gebhardt, K., et al., 1998, AJ, 115, 2285

Makino, J., & Hut, P. 1997, ApJ, 481, 83

McLure, R. J., Kukula, M. J., Dunlop, J. S., Baum, S. A., O'Dea, C. P., & Hughes, D. H. 1999, MNRAS, 308, 377

McLure, R. J., & Dunlop, J. S. 2001, MNRAS, 321, 515

Merritt, D., & Ferrarese, L. 2001, ApJ, 547, 140

Merritt, D., & Ferrarese, L. 2001, MNRAS, 320, L30

Mihos, J., & Hernquist, L., 1994, ApJL, 431, L9

Mihos, J., & Hernquist, L., 1996, ApJ, 464, 641

Mo, H. J., & White S. D. M., 1996, MNRAS, 311, 347

Monaco, P. 1998, Fund. Cosm. Phys., 19, 53

Nagashima, M., Gouda, N., & Sugiura, N. 1999, MNRAS, 305, 449

Nagashima, M., & Gouda, N. 2001, MNRAS, 325, L13

Nagashima, M., Totani, T., Gouda, N., & Yoshii, Y. 2001, ApJ, 557, 505

Nagashima, M., Yoshii, Y., Totani, T., & Gouda, N. 2002, ApJ, 578, 675

Nakamura, T. T., & Suto, Y. 1997, Prog. Theor. Phys., 97, 49

Negroponte, J., & White, S. D. M., 1983, MNRAS, 205, 1009

Netterfield, C. B., Ade, P. A. R., Bock, J. J., Bond, J. R., Borrill, J., Boscaleri, A., Coble, K., Contaldi, C. R., et al. 2002, ApJ, 571, 604

Okamoto, T. & Nagashima, M., 2001a, ApJ, 547, 109

Okamoto, T. & Nagashima, M., 2001b, ApJ in press, (astro-ph/0108434)

Peacock, J. A. & Dodds, S. J. 1996, MNRAS, 280, L19

Pearce F. P., Jenkins A., Frenk C. S., White S. D. M., Thomas P. A., Couchman H. M. P., Peacock J. A., & Efstathiou G. , 2001, MNRAS, 326, 649, (The Virgo Consortium)

Peebles, P.J.E., 1980, The Large-scale Structure of the Universe. Princeton Univ. Press, Princeton

Perlmutter, S., Aldering, G., Goldhaber, G., Knop, R. A., Nugent, P., Castro, P. G., Deustua, S., Fabbro, S., Goobar, A., Groom, D. E., et al., 1999, ApJ, 517, 565

Press, W. H., & Schechter, P. 1974, ApJ , 187, 425

Roukema B. F., Peterson B. A., Quinn P. J., & Rocca-Volmerange B., 1997, MNRAS, 311, 835

Salucci, P., Szuszkiewicz, E., Monaco, P., & Danese, L. 1999, MNRAS, 307, 637

Schmidt, M. 1963, Nature, 197, 1040

Seljak, U. 2000, MNRAS, 318, 203

Shimizu, M., Kitayama, T., Sasaki, S., & Suto, Y. 2002, PASJ, 54, 645

Simien, F., & de Vaucouleurs, G. 1986, ApJ, 302, 564

Somerville, R. S., & Kolatt, T. 1999, MNRAS, 305, 1

Somerville, R. S., & Primack, J. R. 1999, MNRAS, 310, 1087

Somerville, R. S., Primack, J. R., & Faber, S. M. 2001, MNRAS, 320, 504

Springel, V., White, S. D. M., Tormen, G., & Kauffmann, G. 2001, MNRAS, 328, 726

Sugiyama, N. 1995, ApJS, 100, 281

Sutherland, R., & Dopita, M. A. 1993, ApJS, 88, 253

Suzuki, T. K., Yoshii, Y., & Beers, T. C. 2000, ApJ, 540, 99

Takeuchi, T. T., Yoshikawa, K., & Ishii, T. T. 2001, ApJS, 129, 1

Tinsley, B. M. 1980, Fund. Cosm. Phys., 5, 287

Tomita, K. 1969, Prog. Theor. Phys., 42, 9

Thoul, A. A., & Weinberg, D. H. 1996, ApJ, 465, 608

Wang, B., & Heckman, T. 1996, ApJ, 457, 645

White, S. D. M. & Rees, M. J. 1978, MNRAS, 183, 341

White, S .D. M. & Frenk, C. S. 1991, ApJ, 379, 25

Wold, M., Lacy, M., Lilje, P.B., & Serjeant, S. 2001, MNRAS, 323, 231

Yahagi, H., 2002, University of Tokyo PhD Thesis

Yahagi, H., Nagashima, M., Gouda, N., & Yoshii, Y. 2003, in preparation

Yee H.K.C., & Green, R.F., 1984, ApJ, 280, 79

Yee H.K.C., & Green, R.F., 1987, ApJ, 319, 28

York, D. G., Adelman, J., Anderson, J. E. Jr., Anderson, S. F., Annis, J., Bahcall, N. A., Bakken, J. A., Barkhouser, R., et al., 2000, AJ, 120, 1579